Multi-Antenna GPS for Improved Carrier Phase Positioning in Autonomous Convoys

by

Thomas Troupe Tabb

A thesis submitted to the Graduate Faculty of
Auburn University
in partial fulfillment of the
requirements for the Degree of
Master of Science

Auburn, Alabama
August 3, 2019

Keywords: DGPS, Integer Ambiguity Resolution, Multi-Antenna, Convoys, Relative Positioning

Copyright 2019 by Thomas Troupe Tabb

Approved by

David Bevly, Chair, Professor of Mechanical Engineering
Scott Martin, Assistant Research Professor of Mechanical Engineering
John Hung, Professor of Electrical and Computer Engineering
Timothy McDonald, Professor of Biosystems Engineering

Abstract

In this thesis, low-cost differential Global Positioning System (DGPS) techniques are developed for use in automated vehicle convoying. The Global Positioning System (GPS) pseudorange and carrier-phase measurements are used to determine a relative position vector (RPV) between vehicles and between two antennas rigidly fixed to a vehicle in an attitude-baseline configuration. The pseudorange measurements assist in the estimation of the integer ambiguity term inherent in the highly accurate, but ambiguous carrier-phase measurement necessary to achieve centimeter-level relative positioning accuracy. A technique, referred to as Dynamic Base Real Time Kinematic (DRTK) positioning, is described in detail to estimate the carrier-phase ambiguity to ultimately provide a relative position vector estimate between GPS antennas. DRTK is capable of providing relative positioning with L1, L2, and L5 frequencies standalone or in combination with one another. Performance improves with an increasing number of satellites in view and number of frequencies tracked per satellite.

In this thesis, DRTK is aided by including an *a priori* baseline magnitude between antennas in a baseline attitude configuration on a single vehicle as a constraint with a technique referred to as Fixed Attitude-baseline DRTK (FAD). The RPV and relative integer ambiguities between these two fixed antennas, referred to as the base and auxiliary antenna, are computed and used to derive additional measurements between the base antenna and a rover antenna on a separate vehicle via vector addition (FAD+DRTK). This approach improves the availability of the solution by reducing the time-to-first-fix (TTFF) by one half when compared against DRTK with two receivers. A comparative study of FAD+DRTK and the conventional DRTK algorithm is presented when using low-cost single-frequency receivers.

Acknowledgments

This work is dedicated to the memory of my grandmother, Marie Stuart Tabb, the heroine of the Tabb family for nearly eighty years, who urged me to continue my education at Auburn University, April Dean Phillips (favorite mother-in-law), the greatest example of faith, iron-will, and service to others, and my grandfathers, Larry Calhoun and Billy Phillips. I wish to express gratitude to my mother, Kelly, and grandmother, Joann, for their support and encouragement through all of my endeavors, and for reminding me to be a fighter. Thank you to my brothers, Jeb and Cody Tabb, for encouraging me and giving me advice about GPS from their professional lives. It is important for me to also recognize Miss Gay Williams for introducing me to physics and planting the seed that led me to engineering.

Special thanks to Dave Bevly for the opportunity to obtain a Master's degree in the "largest navigation research group in the world" and research a subject I often wondered about all those years operating tractors with GPS guidance systems in the fields of Southwest Georgia for the Sheffield family, to Scott Martin for the initial idea that grew into this work, and to the members of the GAVLAB that made my time at Auburn much more pleasant.

Thank you to John Hung for his wonderful lectures, professionalism, and serving on my committee. Thank you to Tim McDonald for talking to me about tractors, forestry, etc. and turning me and Josh loose in his lab to learn all we would want to know about instrumentation. I express my gratitude to my professors at the University of Georgia, K.C. Das, David Stooksbury, and Ben Davis, for encouraging me to attend graduate school and writing letters of recommendation for my admittance.

Additional words of appreciation are in store for Tanner Ray, Robert Brothers, Dan Pierce, Grant Apperson, Patrick Smith, Stephen Geiger, Ethan Edwards, the Brothers Kamrath and the collective members of the Siberia Office for always being available to borrow hardware, assist in data collection, discuss theory, and their friendship.

Additionally, I am forever indebted to my compassionate father in-law, Stanley Phillips, for his gratuitous financial and emotional support for me and Macy during our sojourn in Auburn. To my Lakeview Baptist Church family, thank you for loving us and teaching us. To Gregg Grimsley, Gerald Garland, and Birdsong Peanuts, thank you for allowing me to attend Auburn to learn a little bit more about engineering, that I hopefully will be able to apply to shelling a peanut, and for holding my job for me until we could come home. Finally, I am eternally grateful for the companionship, love, and comfort provided to me by my wife, Macy, through our times in Bainbridge, Colquitt, Troy, Athens, Damascus, Auburn, and beyond.

Everyone who comes to me and hears my words and does them, I will show you what he is like: he is like a man building a house, who dug deep and laid the foundation on the rock. And when a flood arose, the stream broke against that house and could not shake it, because it had been well built.

(*English Standard Version*, Luke 6:47-48)

Additionally, Go Dawgs.

Table of Contents

List of Figures

List of Tables

Chapter 1

Introduction

One of the main functions of all brains is to take sensory information, use it to generate an estimate of the current state of the world, and then to compare it to the desired state of the world. If the two do not match, compensatory action is initiated, which is what we call behaviour.

–Stanley Heinze [7]

Advancement in autonomous mobility technology has generated great interest in industry and government to apply this technology to vehicle convoy operations to enhance overall convoy performance by reducing specific driving tasks required by operators, improving vehicle control, reducing training time, preventing collisions, and improving safety. In the military, sustainment convoys are imperative for providing adequate supplies and support to personnel across the full range of military operations [8, 9]. Another important result of autonomy in the military is freeing drivers to defend the convoy if under attack by enemy combatants. In industry, autonomous convoying technology shows promise in reducing fuel consumption and greenhouse gas (GHG) emissions, reducing driver fatigue, and eliminating drivers entirely when full autonomy is reached [10, 11].

The ultimate goal of autonomous convoying is to essentially revert to the convenience of traveling by rail without the burden of laying physical tracks; rather, autonomous convoys operate by following a path determined by a *leader*. To continue the railroad analogy, one may think of the lead vehicle as a locomotive. Just as a rail car follows the railroad tracks, the vehicles behind the leader, *followers*, traverse the path laid by the leader. The objective of a follower is simply to follow the path of the leader smoothly and at a distance that achieves

Figure 1.1: Auburn University trucks in a convoy configuration during testing on forest roads in Canada.

mission specific goals or allows the follower(s) to reduce experienced drag to minimize fuel consumption. A depiction of the configuration of an autonomous convoy is given in Figure 1.1.

1.1 Vehicle Sensing for Autonomous Convoying

Navigation is the field of study that focuses on the process of monitoring and controlling the movement of an aircraft or ground vehicle from one place to another [12]. Navigation requires knowledge of where one is and where one aims to be. Knowledge of one's location is described in relation to a reference. This reference can be global or local. *Positioning* is the ability to accurately and precisely determine one's location and orientation two-dimensionally or three-dimensionally when required, referenced to a standard geodetic system. *Relative positioning*, in the context of this thesis, is knowing where a follower is in relation to the leader once the leader has been identified. The leader is *localized* to its environment or positioned globally. According to Huang & Dissanayake [13], "Robot localization is the process of determining where a mobile robot is located with respect to its environment. Localization is one of the most fundamental competencies required by an autonomous robot

as the knowledge of the robot's own location is an essential precursor to making decisions about future actions." To achieve these lofty goals, a variety of sensors have been utilized with varying degrees of accuracy to provide valuable positioning and localization information to navigate the autonomous vehicle. Sensors commonly used in vehicle positioning and navigation systems are typically broken into two distinct categories: absolute and relative sensing [14]. Before beginning discussion of the topic of this thesis, a brief survey of sensing technologies commonly used in the field of autonomous mobility is presented.

1.1.1 Absolute Sensing

Absolute heading and position sensors are incredibly useful for solving positioning and navigation problems. Absolute measurements are needed because a relative sensor alone is not capable of providing an absolute orientation or position with respect to a reference. The purpose of absolute sensing is to provide information about the vehicle's orientation and location with respect to a reference such as the Earth. The most common sensors to achieve global positioning are the magnetic compass and the Global Positioning System (GPS) [15].

1.1.1.1 Magnetic Compass

Heading is the most significant navigation parameter in regard to its influence on accumulated dead-reckoning errors [14]. Magnetic compasses use a measurement of the Earth's magnetic field to determine the orientation of vehicles, airplanes, and even Boy Scouts. The first magnetic compasses were constructed over 2,000 years ago during the Han Dynasty in China with lodestone, a naturally magnetized stone of iron [16]. A typical magnetic compass is capable of providing a measurement of absolute heading with a precision of 0.1° and an accuracy of 0.5° [14]. Orientation is measured with respect to Magnetic North.

Magnetometers are a commonly used sensor in robotics that measures the Earth's magnetic field. In conjunction with a three-axis accelerometer, a three-axis magnetometer can be used as a magnetic compass to determine heading with respect to Magnetic North. For

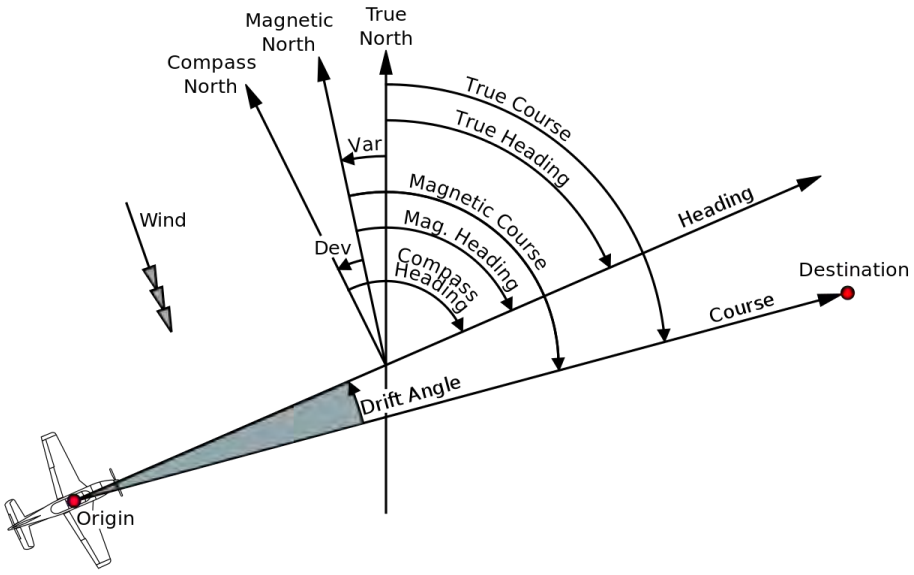

Figure 1.2: Description of heading provided by a magnetic compass on an aircraft.

successful implementation, certain application specific limitations must be addressed. Vehicles are partially made of ferrous materials that distort the Earth's magnetic field, along with components that produce a magnetic field (e.g. speakers, electric motors, seat warmers, window defrost strips, etc.). Magnetometers measure the vector sum of all magnetic fields present; therefore, the compass must be calibrated appropriately and monitored for errors caused by long-term magnetic anomalies with an external reference (e.g. GPS, differential odometer, International Geomagnetic Reference Field (IGRF), or World Magnetic Model (WMM)). Additionally, it is beneficial for the magnetometer to operate at a level attitude as much as possible. This may be achieved by gimbal-mounting the magnetometer to prevent errors introduced by the vertical component of the geomagnetic field or using an external attitude reference for correction [14]. The reader is directed to [15] for a more thorough discussion about the application of magnetic compasses in vehicle navigation.

1.1.1.2 Global Positioning System

Figure 1.3: An early navigator making use of a sextant.

For thousands of years, humans have used the natural stars for navigation. Navigators used a device called a *sextant* (see Figure 1.3) to make angular measurements to stars from the horizon. This technique is known as celestial navigation, which uses the method of *triangulation* to determine position by angular measurements. Over a long Labor Day weekend in 1973, a group of armed forces officers and civilians gathered in the Pentagon were completing a plan that would revolutionize navigation. Rather than using angular measurements to a celestial body, this system would use radio ranging to a constellation of artificial satellites called *NAVSTARs* [17]. Determining one's position based on distance measurements to the artificial NAVSTARs is known as *trilateration*. GPS can provide service to an unlimited number of users since the user receivers operate passively (i.e. receive only) [5]. The system provides users the ability to determine their position, velocity, and synchronize their clocks with GPS time with the only prerequisite being an appropriate receiver. To determine position, a minimum of four of the thirty-one active satellites in the GPS constellation, as of the time of this writing, must be in view for the receiver to resolve the unknowns of latitude, longitude, altitude, and correction to the user's clock. The United States is committed to maintaining the availability of at least 24 operational GPS satellites 95% of the time. The current *Global Positioning System Standard Positioning Service Performance Standard* release by the Pentagon in 2008 specifies a 2-σ accuracy of 7.8 m during normal operation over all ages of Ephemeris data, which is the data used to estimate the location of satellites, using a simple single-frequency receiver [18]. In practice, standalone positioning accuracy with a GPS receiver is typically 3 m. However, a costlier dual-frequency receiver combined with a correction service (e.g. real time kinematic (RTK)), this accuracy can reach centimeter level [19]. Not only does GPS offer global position solutions, multiple antennas may be fixed in an attitude configuration on a vehicle to determine attitude (i.e. heading, pitch and roll). The problems associated with using GPS for navigation are signal blockage, multipath interference, and jamming or spoofing by adversaries [14]. A thorough discussion of GPS will be provided in Chapter 2.

Figure 1.4: Two Navcom SF-2040G StarFire GPS receivers, along with a Garmin 12XL handheld. The Navcom on the right is using a Bluetooth serial adaptor.
Source: [1]

1.1.2 Relative Sensing

Relative, or displacement, sensors give the user a measurement of the change in distance, velocity, or orientation with respect to a previous measurement [15]. In a word, apart from vision-based relative position sensing, relative position sensors are proprioceptive. Proprioception, in the biological context, is the sense of self-movement and body position [20]. As an illustration, imagine a blindfolded person on a turntable that can translate and rotate placed in an unfamiliar location. As the turntable changes orientation and position, an assistant will say how much the turntable rotates and translates while the blindfolded subject will record this information. At the end of the experiment, the blindfolded person can easily give a history of their movement and where they are in relation to their starting point but will be incapable of providing an accurate location apart from which city, county, country, or planet they may inhabit. This describes the concept of *dead-reckoning*. However, if the assistant gives the blindfolded person their absolute starting location and orientation provided by GPS and a magnetic compass, the blindfolded person can also determine where they are located. Dead-reckoning has been used for ages. Early European explorers like

Christopher Columbus and Vasco de Gama used this technique to navigate to and from the New World by recording their movements in relation to the port they departed [21].

1.1.2.1 Odometry

Odometry is the one of the most commonly used sensors for vehicle positioning [14]. Its strengths are satisfactory short term accuracy, affordability, and high sample rate. The issues lie in the inherent necessity to integrate successive motion history to provide information about distance traveled. If any prior measurement is inaccurate, this error will propagate and accumulate without bound. For instance, orientation errors lead to large errors in lateral position that increase proportionally to distance traveled. The typical sensor used in odometry of wheeled vehicles is a rotary encoder, a electro-mechanical device that converts the angular position or motion of a shaft to analog or digital signals. This information combined with knowledge of the radius of the wheel provides a measurement of linear translation. Note that this measurement is dependent upon the radius of the wheel and the assumption that the wheel does not slip. The rotary encoder shown in Figure 1.5 is an example of an encoder likely to be found on a unmanned ground vehicle (UGV).

With pneumatic tires, this radius is at the mercy of temperature and loading which can effect the effective radius of the wheel. Additionally, wheeled vehicles are expected to experience wheel slip which is typically dependent on load, inflation pressure, and velocity [22]. Quantifying odometry measurement errors is not well-defined. These measurement errors are separated into two groups: systematic and non-systematic. Systematic errors are errors in the kinematic model and non-systematic errors are errors arising from the uncertainty in the interaction between the wheels and driving surface. To address these errors, Borenstein and Fang developed methods in [23, 24] to measure systematic and non-systematic errors; unfortunately, these methods depend on information about the surface driven and a predefined square path that is unlikely to be available to autonomous vehicles required to operate in many diverse environments.

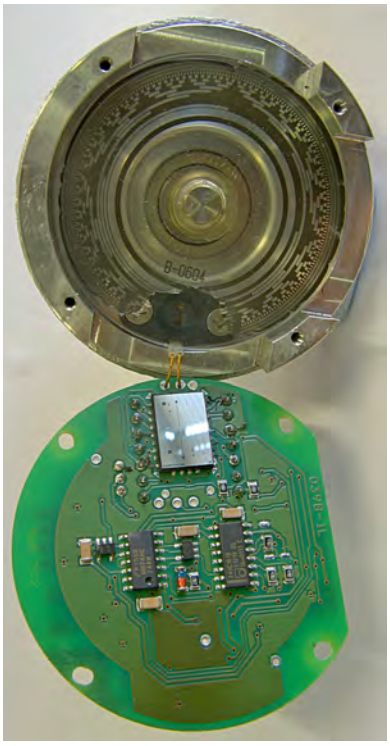

Figure 1.5: An example rotary encoder used to provide odometry measurements.

GPS may also be leveraged to provide an odometry measurement independent of the aforementioned systematic and non-systematic errors. A technique known as time difference carrier-phase (TDCP) odometry can be used to track changes in a GPS receiver's motion with high accuracy but at a lower sampling rate than a rotary sensor. TDCP odometry is achieved by differencing successive GPS carrier-phase measurements in time to remove time correlated errors. TDCP is capable of providing odometry measurements at the sub-centimeter level; however, TDCP performance is subject to satellite visibility, satellite geometry, and GPS receiver quality [25] .

1.1.2.2 Inertial

An inertial measurement unit (IMU) is comprised of three mutually orthogonal accelerometers and gyroscopes. Gyroscopes measure angular rate about each orthogonal axis. The first apparatus similar to a gyroscope was developed by the English sea captain John Serson in 1743 [26]. Léon Foucault, the very same Foucault that developed the Foucault

pendulum that can be seen as a reproduction on Auburn University's campus in Ross Hall, appropriated a device developed by Walter R. Johnson to observe the rotation of the Earth and gave the device its modern name, gyroscope [27]. Accelerometers measure proper acceleration in the direction of each sensitive axis, which is the same acceleration that humans experience in relation to an inertial frame [28], [29].

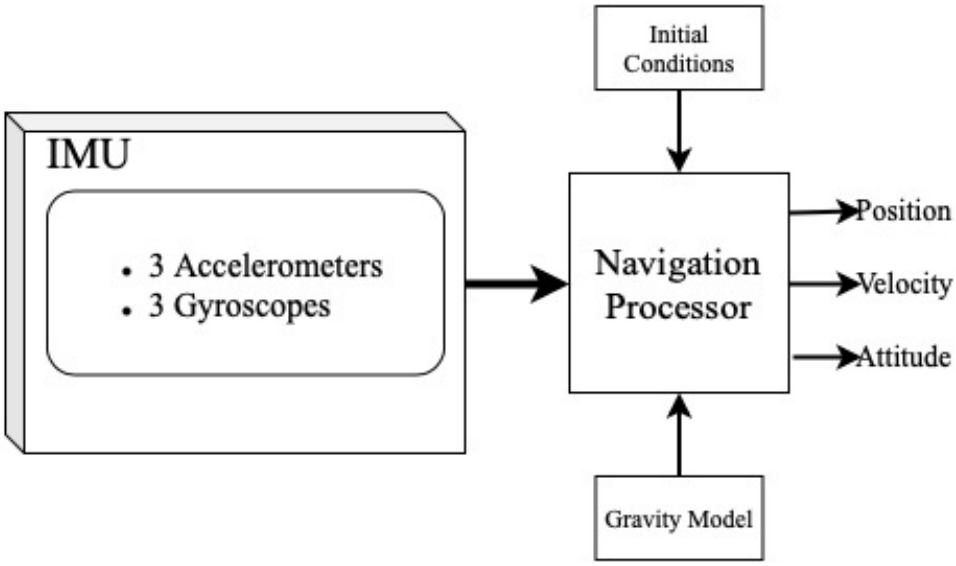

Figure 1.6: Schematic of an inertial navigation system.

An inertial navigation system (INS) is a complete three-dimensional dead-reckoning navigation system comprised of the aforementioned IMU and a navigation processor as described in Figure 1.6. The INS is able to provide navigation solutions at a high rate (e.g. hundreds of times per second); however, like all dead-reckoning sensors, error grows without bound as successive accelerometer and gyroscope errors are summed if not corrected by external aiding. INS performance can vary by several orders of magnitude, depending on the quality of the accelerometers and gyroscopes. The best INSs are reserved for use in ships, submarines and select spacecraft. The INSs used by commercial airliners and military aircraft experience a horizontal drift of less than 1,500 m over the first hour and cost around $100,000. The cheapest and smallest inertial sensors, microelectromechanical systems (MEMS), are suitable for inertial navigation in vehicles and pedestrian dead-reckoning

(PDR) with external aiding (e.g. GPS) [4]. Recent work in PDR developed by the GPS and Vehicle Dynamics Laboratory (GAVLAB) at Auburn University may be found in [30, 31]. Inertial sensors for vehicle navigation are typically installed in the strapdown configuration that aligns the accelerometers with the navigating body with care to minimize misalignment errors. Other common errors inertial sensors experience are inherent bias, scaling, and random noise. The dominant error source for inertial sensors is often bias. Typical values of internal bias for different IMU grades is given in Table 1.1.

GPS performance is limited by signal outages and low sampling rates (e.g. 10 Hz) but provides long-term accuracy. INS performance is limited by error drift, thus provides short-term accuracy may be sampled quickly (e.g. 100 Hz). The drawbacks of inertial sensors and GPS are complementary, so by combining them, the advantages of the two technologies are offered to provide a continuous, high-bandwidth, complete navigation solution with high long and short-term accuracy. This is commonly referred to in the literature as GPS/INS integration. The GPS measurements provide corrections to correct error drift in the INS, while the INS can smooth the GPS solution and bridges brief GPS signal outages [4]. Additionally, gyroscopes alone are incredibly useful in positioning because they can assist in compensating for the foremost weakness of odometry: any small momentary orientation error will cause a constantly growing lateral position error [14].

Table 1.1: Representative Bias Values for Different IMU Grades (From: [4])

IMU Grade	**Accelerometer Bias** (m/s^2)	**Gyroscope Bias** (deg/hr)
Marine	10^{-4}	0.001
Aviation	3×10^{-4}–10^{-3}	0.01
Intermediate	10^{-3}–10^{-2}	0.1
Tactical	10^{-2}–10^{-1}	1–100
Automotive	>1	>100

1.1.2.3 Vision

In recent years, both video and light detection and ranging (LiDAR) sensors have been deployed to determine the position of a leader vehicle, and identify obstacles and other important objects in the environment [32]. Additionally, radio detection and ranging (RADAR) sensors are also used to determine the relative position of a leader vehicle. These sensors have proven useful for tackling the problem of Simultaneous Localization and Mapping (SLAM), which is the task of a mobile robot building a map of an unknown environment while simultaneously navigating through the environment using said map [33]. This problem was first addressed in the mid-80s in the seminal work on SLAM by Chatila and Laumond in [34]. Feŕaud et al. implemented this technique in a convoy configuration and were able to localize the follower vehicle in a 3D map with an accuracy of 10 cm.

The primary drawback of these sensors is maintaining line-of-sight (LOS) with the target (i.e. the leader vehicle). Additionally, LiDAR and cameras are susceptible to adverse environmental operating conditions (e.g. smoke, fog, dust, rain, snow). All of the vision-based sensors are also limited to operate within approximately 800 m of the leader vehicle, for radar, and less than 100 m for LiDAR [35]. For a more thorough discussion of vison-based sensing in autonomous convoys, the reader is directed to [8, 10, 14, 35–38].

1.2 Prior Work

Now that there has been a through review of sensing technologies commonly used in mobile robotic positioning, and more specifically, autonomous convoying, the topic of this thesis may be discussed in a more intelligible context. It is important to note that in the field of autonomous convoying, a multi-sensor approach yields better performance, because no sensor alone is perfectly suited for such a complex problem [39]. DRTK is an application of the technique of differential GPS (DGPS). DGPS removes correlated errors between two receivers, with one located at a well-surveyed location, to provide a highly accurate global positioning solution by leveraging the highly accurate, but ambiguous, carrier-phase

measurement. Carrier based positioning was first explored in the 1970s. The first use of carrier-phase measurements for positioning in a dynamic application was in 1985 [40]. The carrier-phase measurement will be discussed in Chapter 2. A good resource describing DGPS is in [17]. The next advancement in satellite-based navigation was the advent of real-time kinematic positioning (RTK) in the early 1990s that allows a user to receive corrections to provide a highly accurate global position in real-time rather than in post-process [41]. Previous work in the area of formation flight [42, 43], automated aircraft refueling, [44], and the Joint Precision Approach and Landing System (JPALS) [45] developed methods to produce relative positioning information with accuracy similar to RTK. Ultimately, the shoulders on which this thesis work stands is that of the DRTK technique developed at Auburn University [46, 47]. The DRTK algorithm will be discussed in detail in Chapter 3.

This thesis incorporates measurements from three GPS receivers to improve the performance of the conventional DRTK technique where only two receivers are used. This thesis work was inspired by Sperl in his Master's thesis at Technische Universität München in Germany. He showed that RTK with a virtual base station can be improved by incorporating measurements from three antennas via vector addition with a known, rigidly fixed baseline between two antennas once the integer ambiguity term and relative position vector between the fixed baseline is resolved [48] . Additionally, Clark Cohen showed in [17] that including a constraint of the *a priori* magnitude of the vector between two fixed antennas aids in integer ambiguity resolution. Ultimately, the work of Sperl and Cohen led to the work of improving the performance of DRTK when using low-cost single-frequency GPS receivers.

1.3 Contributions

The purpose of the research presented in this thesis is primarily to improve the performance of the DRTK algorithm's objective of providing a 3D relative position solution in an autonomous convoy. With this in mind, the following contributions are made:

- *A priori* baseline magnitude information is used to constrain the estimate of integer ambiguities between two GPS antennas to provide a high precision relative position vector (HPRPV). The constrained and unconstrained estimator are compared.

- Relative positioning algorithms incorporating measurements from three GPS antennas with two in an attitude baseline configuration, and one acting as a rover, are developed to provide RTK quality relative position solutions without a static base station. The multi-antenna approach is compared to conventional DRTK with two receivers.

- The constrained estimator and the multi-antenna measurement approach are used to improve the performance of DRTK with low-cost single-frequency receivers.

1.4 Thesis Outline

Beginning with a discussion of the history and development of GPS in Chapter 2, this thesis continues discussion of the GPS signal structure and expected measurement errors. Next, in Chapter 3, the DRTK algorithm is introduced with an explanation of the Least Squares Decorrelation Adjustment Method (LAMBDA) for fixing float integer ambiguity estimates to integers. To conclude Chapter 3, an explanation of the determination of a high precision relative position vector (HPRPV) describing the relative position with *cm* level accuracy is presented along with experimentation and results with this technique.

The main contributions of this thesis are presented in Chapters 4 and 5. Chapter 4 details the *a priori* baseline magnitude constraint used to more rapidly resolve integer ambiguity terms by constraining the estimates of the integer ambiguity terms in a linear, discrete Kalman filter framework. The technique applied to DRTK is presented followed by experimentation and results. Chapter 5 discusses improvements in the DRTK solution with low-cost single-frequency receivers provided by additional derived measurements. Finally, Chapter 6 discusses future work in this approach and conclusions.

Chapter 2

The Global Positioning System

GPS in many ways is like the Internet. Both are gifts of the U.S. Department of Defense to the civil world. Both continue to transform the way we do ordinary, everyday things as individuals and society, delivering wide-ranging economic and social benefits far beyond anything their designers could have dreamed of.

–Pratap Misra and Per Enge [21]

The initial principle purpose of GPS was to offer the U.S. military accurate estimates of position, velocity, and time (PVT). These estimates were to be accurate to 10 m for position, 0.1 m/s for velocity, and 100 ns for time, all in the root-mean-square (rms) sense, and were to be made available to an unlimited number of U.S. Department of Defense (DoD)-authorized users globally, continuously, and instantaneously via the *Precise Positioning Service* (PPS) [21]. Additionally, the DoD planned to provide civil users of GPS a lower quality positioning service, *Standard Positioning Service* (SPS), that was consistent with national security considerations. The DoD achieved this by corrupting the civilian signal with controlled errors via a feature called *Selective Availability* (SA). GPS was declared operational in 1995 and exceeded the expectations of the service promised in its initial performance specifications [18]. In 2000, a Presidential Order deactivated SA to provide civilian users standalone positioning to an accuracy of around 3 m, rather than the accuracy of 100 m provided under SA corruption. With this level of accuracy for civilians, the applications for civil use of GPS expanded and continues today.

2.1 System Architecture

GPS consists of three segments: the Space Segment, the Control Segment, and the User Segment. The Space Segment is comprised of the satellites, the Control Segment manages satellite operations, and the User Segment is related to the development of civilian and military GPS user hardware. A brief description of each segment's function is provided below.

2.1.1 Space Segment

The space segment is the constellation of satellites (i.e. space vehicles (SV)) that provides the signals from which users make ranging measurements. The SVs transmit a pseudorandom noise (PRN)-coded signal unique to each SV known as the coarse/acquistion code (C/A) from which the ranging measurements are made. As stated earlier, this is a passive architecture. This ranging signal is also modulated with data that provides information that defines the positions of the satellites. Additionally, each SV includes payloads and vehicle control subsystems. One payload supports the original GPS position, velocity, and time (PVT) mission; the other payload detects Earth-based radiation phenomena to serve as a nuclear detonation detection system. The vehicle control system corrects the SV orbit and SV orientation to maintain direct signal transmission to Earth and to ensure the on-board solar panels are directed to the Sun [5].

The constellation was designed to provide all users with a clear view of the sky a minimum of four SVs in view; fortunately, it is more likely to see six to eight SVs at any time in practice. The constellation is currently comprised of 31 active SVs in six orbital planes (A through F), all with inclination angles of 55° relative to the equatorial plane. Each orbital plane is comprised of at least four SVs. The orbits are nearly circular with a radius of 26,560 km measured from the center of Earth. Finally, each SV is identified by its unique PRN number [21]. See Figure 2.1 for a visualization of the orbits and Table A.1 in the Appendix for a list of active satellites.

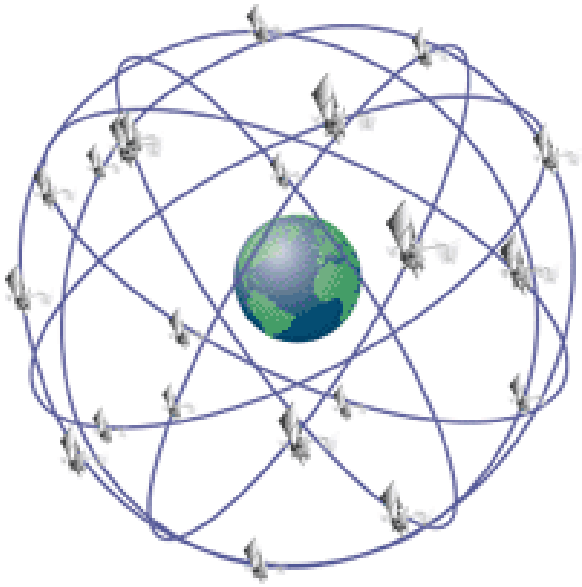

Figure 2.1: Depiction of the GPS orbits.

2.1.2 Control Segment

The Control Segment is comprised of a Master Control Station (MCS) and seventeen monitoring stations around the Earth responsible for monitoring, commanding, and controlling the Global Positioning System. Figure 2.2 gives a map of the elements of the Control Segment. The head of the Control Segment is the MCS at Schriever Air Force Base near Colorado Springs, Colorado. The MCS operates the system and provides command and control functions. The specific functions of the Control Segment are:

- to monitor satellite orbits,
- to monitor and maintain satellite health,
- to maintain GPS time,
- to predict satellite ephemerides and clock parameters,
- to update satellite navigation messages,

- to command small maneuvers of satellites to maintain orbit, and relocations to compensate for failures, as needed [21].

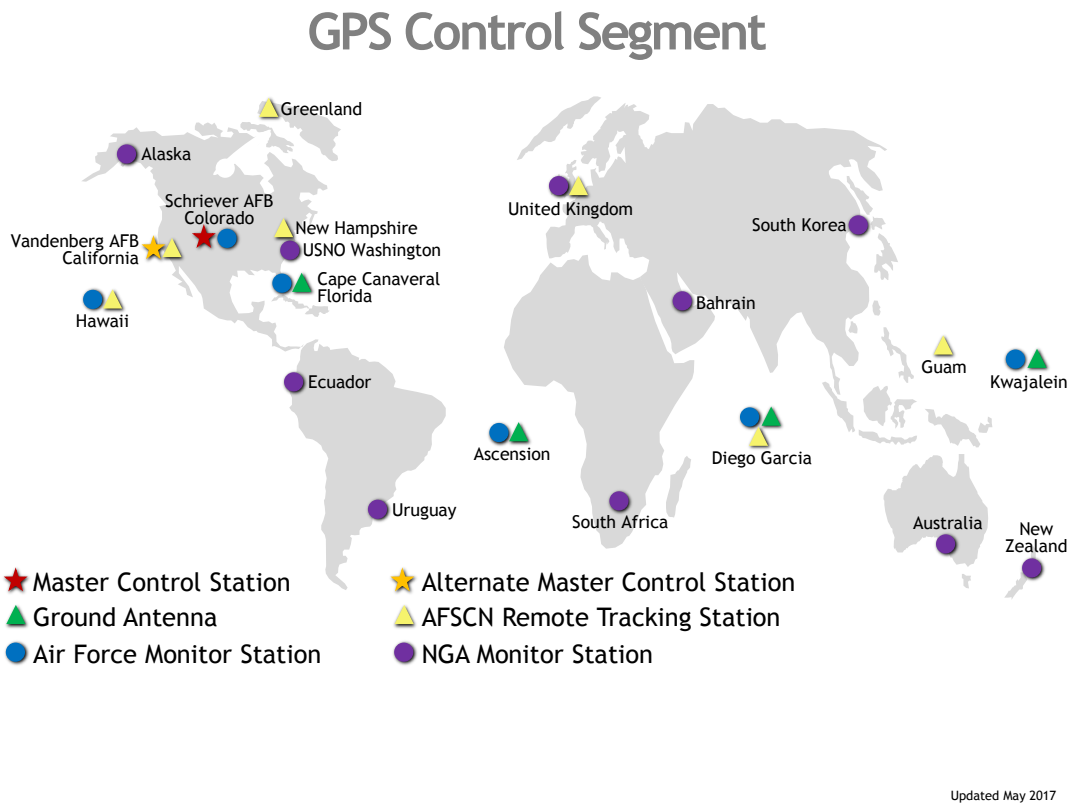

Figure 2.2: Map of the elements of the Control Segment. Source: [2]

2.1.3 User Segment

The User Segment is comprised of the hardware required to capture the radio frequency (RF) signals emitted by the SVs and perform calculations to estimate the user PVT. The hardware required is a GPS receiver and antenna. Early receivers produced in the mid-1980s were priced upwards of $100,000. In 1992, the first hand-held receiver could be purchased for less than $1,000; in 1997, the industry broke below $100 for a pocket-sized receiver powered by two AA batteries [21]. Today, survey-grade receivers range in price from $5,000-$30,000 or more. Low-cost single-frequency receivers can now be purchased for as low as $50.

Signals are received by the GPS antenna, which provides near hemispherical coverage (e.g. 160°). Most GPS antennas have a built-in pre-amplifier that may be powered externally or more commonly by the receiver's RF coaxial cable. GPS antennas vary in cost from as low as $5 for a passive antenna to several thousand dollars for a high-quality choke ring antenna (see Figure 2.3) capable of rejecting erroneous reflected signals known as *multipath*.

Figure 2.3: Trimble choke ring antenna. Source: [3]

Given data describing current SV locations and a rough idea of user location, the receiver determines which SVs are in view. With knowledge of the SV IDs, the receiver knows the PRN code unique to each SV and attempts to align the receiver generated replica of the

known PRN code to acquire the signal. After successful acquisition, the receiver uses a feedback control loop (i.e. delay lock loop (DLL)) to continuously adjust the replica code to maintain alignment with the incoming PRN code. The time shift discovered in this process is multiplied by the speed of light to give the *pseuodrange* measurement. The time shift is essentially comparing the user's clock time at arrival to the SV clock time at transmission. Additionally, after the alignment is successful, the PRN code is removed from the signal, leaving only the navigation (NAV) message. The navigation message of each SV contains the Ephemeris data necessary to calculate its own accurate location, time parameters and clock corrections, and Almanac data necessary to roughly calculate the positions of all SVs in the constellation. After PRN removal, the signal is now tracked with another feedback control loop called a phase lock loop (PLL). Similarly, the receiver generates a sinusoidal signal to match the frequency and phase of the incoming signal, and extracts the navigation message. A depiction of L1 GPS carrier signal with modulation is shown in Figure 2.4.

Most importantly for the topic of this thesis, the *carrier-phase* measurement is made in the PLL by measuring the initial fractional phase difference between the received and receiver-generated signal, and then tracking changes in the signal phase by counting whole cycles and keeping track of the fractional cycle at each measurement epoch. The total number of whole cycles between the receiver and the SV is unknown. This is known as the *integer ambiguity*. This measurement is much less noisy than the pseudorange measurement and can provide centimeter level positioning accuracy once the integer ambiguity is determined [17]. This process is known as *integer ambiguity resolution* and the foundation of this thesis is to describe methods to resolve the integer ambiguity.

2.1.3.1 Measurement Models

The two measurements of note in this thesis are the pseudorange and carrier-phase measurement. In estimation and control, it is essential to have a good understanding of the model of the system of interest. The models used in this thesis are those as described by

Misra and Enge in their popular textbook [21]. The measurement models of the pseudorange and carrier-phase measurement are given below in Equations (2.1) and (2.2), respectively.

$$\rho_u^j = ||\mathbf{r}_u^j|| + c(\delta t_u - \delta t^j) + T^j + I^j + \eta_u^j \tag{2.1}$$

$$\phi_u^j = ||\mathbf{r}_u^j|| + c(\delta t_u - \delta t^j) + T^j - I^j + +\lambda N^j + \epsilon_u^j \tag{2.2}$$

The variables are defined as follows:

- ρ_u^j is the pseudorange measurement between the user receiver, u, and the SV, j, in units of m.
- ϕ_u^j is the carrier-phase measurement between the user receiver, u, and the SV, j, in units of m after scaling the integer ambiguity term, N^j, by the carrier signal's wavelength, λ.
- $||\mathbf{r}_u^j||$ is the true range magnitude between receiver, u, and SV, j, in units of m.
- λ is the carrier signal wavelength in m.
- I is the ionospheric delay/advancement in units of m.
- T is the tropospheric delay in units of m.
- δt_u,δt^j are the clock errors, in s, at the receiver, u, and the SV, j.
- N^j is the integer ambiguity term in cycles from receiver, u, to SV, j.
- η_u^j is the system noise on the pseudorange measurement including multipath.
- ϵ_u^j is the system noise on the carrier-phase measurement including multipath.

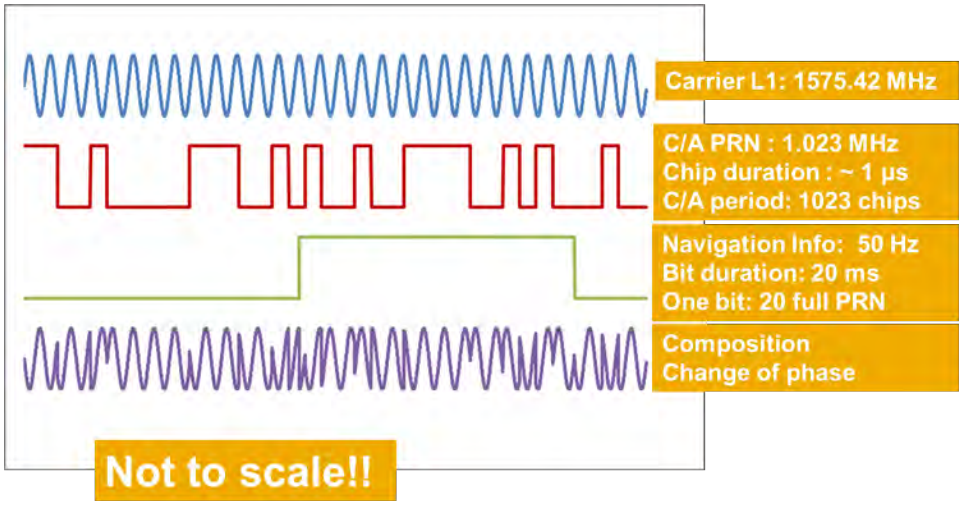

Figure 2.4: Description of the L1 GPS carrier signal with data modulation.

2.2 Error Sources

2.2.1 Measurement Errors

The nondeterministic component of the measurement error is the system noise and multipath. All other nonparametric components can be modeled or estimated. The noise on the measurements can be quantified by determining the accuracy of the DLL and PLL within the receiver as a function of the carrier to noise ratio, C/N_0. The accuracy of both measurements decreases with decreasing C/N_0. The standard equations to estimate DLL and PLL accuracy are given in (2.3) and (2.4) [5].

$$\sigma_{DLL} = \lambda_c \sqrt{\frac{4d^2 B_{n\rho}}{C/N_0}\left(2\left(1-d\right) + \frac{4d}{T_s C/N_0}\right)} \tag{2.3}$$

$$\sigma_{PLL} = \frac{\lambda}{2\pi}\sqrt{\frac{B_{n\phi}}{C/N_0}\left(1 + \frac{1}{T_s C/N_0}\right)} \tag{2.4}$$

The DLL and PLL tracking loop parameters are receiver dependent; for this work, approximations were made based on those given in [5]. These values can be found in Table 2.1. A common approximation for a high-quality receiver is that measurements can be made

Table 2.1: Tracking Loop Parameters. (From: [5])

Parameter	**Description**	**Value**	**Unit**
$B_{n\rho}$	Code loop noise bandwidth	2	Hz
$B_{n\phi}$	Carrier loop noise bandwidth	18	Hz
C/N_0	Carrier to noise ratio	variable	Hz
d	Correlator spacing	0.5	$chips$
λ	Carrier wavelength	L1: 0.1902 L2: 0.2442	m
λ_c	Code chip width	C/A: 293.05	m
T_s	Predetection integration time	0.005	s

with accuracy to 1-2% of the signal wavelength. The C/A code from which the pseudorange measurement is determined, has a wavelength of roughly 300 m and the carrier wave from which the carrier phase measurements are determined, have wavelengths of 19 cm and 24 cm for the L1 and L2 carrier frequencies, respectively. After accounting for noise and resolution error, the 1σ values for the pseudorange measurement and carrier phase measurement are 1.5 m and approximately 3 mm, respectively [5].

2.2.2 Signal Modeling Errors

The GPS signal travels through a vacuum for approximately 95% of its travel distance from the SV to the user receiver near Earth, which corresponds to a travel distance of about 20,000 km when the SV is directly overhead to about 26,000 km when the SV is setting or rising at the horizon. The roughly 5% of travel distance through the atmosphere is where the signal's propagation is altered. The first layer of the atmosphere that alters the signal is the *ionosphere*, which consists of a layer of charged particles. The next layer altering the signal is the *troposphere*, a layer of electrically neutral gases. These layers change the speed and direction of the signals by a phenomenon known as *refraction*. Refraction of the signal changes the signal transit time, which affects the estimated range measurement. The *refractive index* of a medium, n, is defined as the ratio of the speed of propagation of a signal in a vacuum (e.g. the speed of light, c) to the speed in the medium, ν, given in (2.5).

$$n = \frac{c}{\nu} \tag{2.5}$$

If the refractive index of a medium depends upon frequency of the signal, the medium is *dispersive*. The ionosphere is a dispersive medium. The ionospheric advancement/delay may be modeled with ionospheric model parameters given in the NAV message. Additionally, if the user is equipped with a dual-frequency (L1-L2) receiver, the ionospheric advancement/delay may be estimated by the measurements provided by the different frequency signals. These techniques are described in detail in Section 5.3.2 in [21]. The troposphere is less troublesome than the ionosphere. The unaccounted ionosphere can cause a delay of several tens of m; while the troposphere causes a delay of a couple m. Of the many models used to estimate the tropospheric delay, the *Saastamoinen model* is quite common [21]. The estimation of tropospheric delay is based upon average meteorological conditions specific to the user location for the year. A visual representation of the effects of the troposphere and ionosphere on the GPS signal is given in Figure 2.5.

2.2.3 Control Segment Errors

The Control Segment sends Ephemeris and SV clock parameter values that are broadcast by the SVs. These parameters are computed by the Control Segment on the basis of measurements at GPS monitor stations in a Kalman filter framework. A prediction model is then used to generate Ephemeris and clock parameters to be uploaded to the SVs to broadcast in the NAV message. As in all estimation attempts, there are errors with both the estimation of the current and future parameters. The error grows with the age of data (AoD), defined as the time since the last parameter upload. The root-mean-square (rms) ranging error attributed to the Control Segment is approximately 3 m [21].

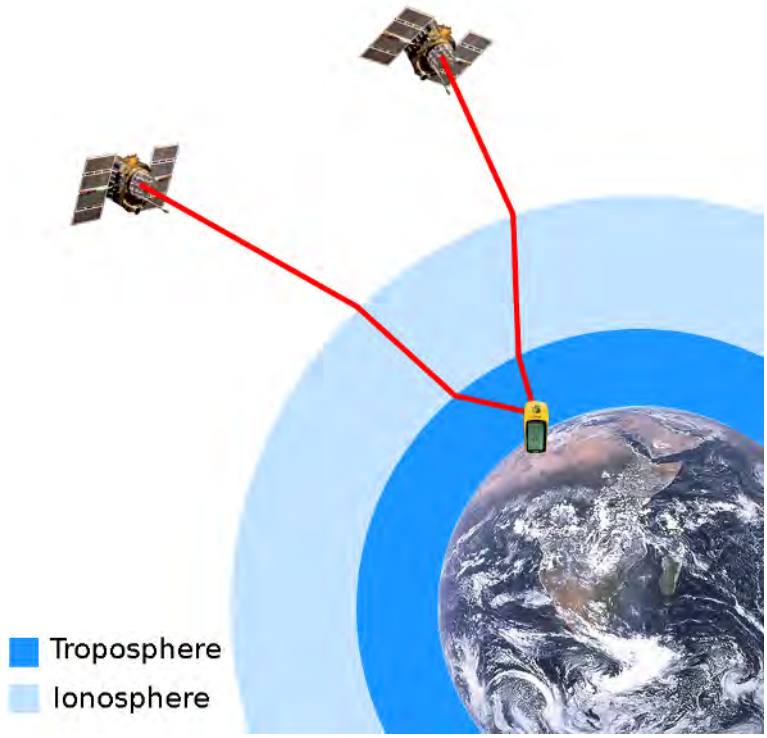

Figure 2.5: The effect of the troposphere and ionosphere on GPS signals

2.2.4 Experimentation and Results

To observe the expected positioning error, 50 min of data taken at 1 Hz was collected by a static patch antenna atop the Woltosz Engineering Research Laboratory on the campus of Auburn University. The receiver used was a dual-frequency NovAtel OEM3 ProPak. The collected data was compared against RTK truth. As expected, the total standalone positioning accuracy was nearly 3 m. The receiver achieves this with a combined approach of signal processing and atmospheric modeling to remove some of the errors discussed in this Chapter [49]. The statistical results of this experiment are tabulated in Table 2.2, and the error in solution at each sample time are displayed in Figure 2.7. The coordinate frame used was Earth-Centered Earth-Fixed (ECEF). A description of this coordinate system is given in Appendix B. The solution provided at every epoch is shown geographically atop the Woltosz Engineering Research Laboratory roof in Figure 2.6.

Figure 2.6: Receiver reported standalone positioning solutions.

Table 2.2: Error statistics from 50 minutes of receiver reported position compared with RTK.

	RMSE (m)	Var (m^2)
x	0.729	0.526
y	0.856	0.709
z	0.846	0.593
Total	2.430	1.8290

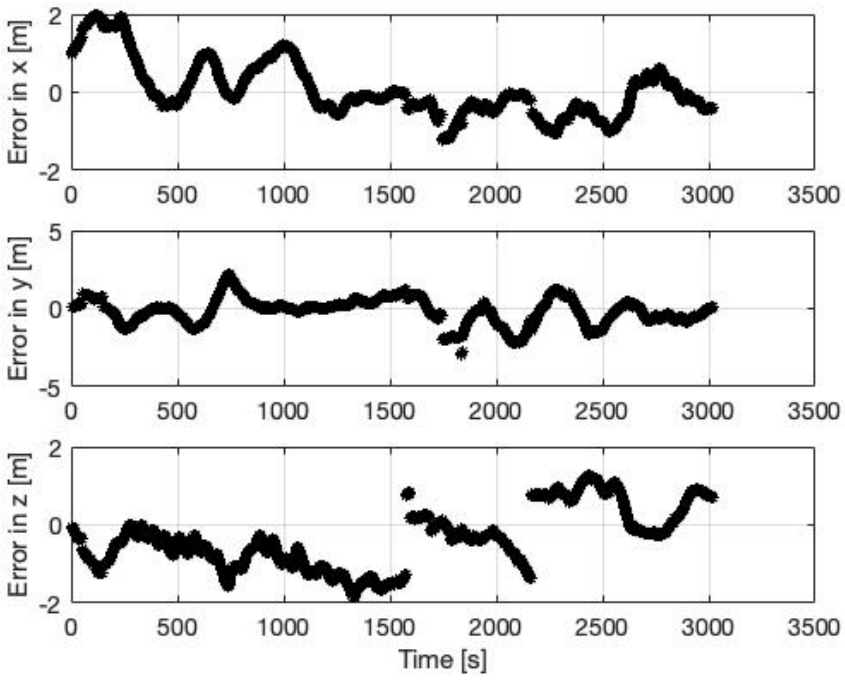

Figure 2.7: Error in receiver reported standalone positioning solutions.

Chapter 3

Dynamic Base Real Time Kinematic Positioning

Chapter 2 described the error sources of the pseudorange and carrier-phase measurement. A careful reader will notice that some of the error sources for each measurement are dependent upon the receiver's location (e.g. T^j, and I^j) and one of the error sources is unique to each SV (e.g. δt^j). In theory, these error sources are common to two receivers roughly in the same location. In fact, these error sources can be estimated by a well-surveyed, static *base* receiver roughly in the same location (i.e. within 20 km) as the *user* receiver. The base receiver can send error corrections to the user receiver to correct the pseudorange measurement. This technique is referred to as *code-phase DGPS*. *Carrier-phase DGPS* differences carrier-phase measurements between the base and user receiver to remove correlated errors and resolve the remaining integer ambiguity term to provide a user position accurate to a couple of cm [17]. The trouble with these approaches is the necessity for a static, well-surveyed base station to provide an accurate absolute position. In applications where an accurate *relative position* is desired, DRTK may be used to provide the same level of accuracy as carrier-phase DGPS [47].

3.1 DRTK

The DRTK technique described in this thesis is based upon the work done by various authors in [42–45] and further developed at Auburn University by Travis et al. in [46, 47]. DRTK is a DGPS technique that provides cm level relative positioning accuracy without a static base station. This is advantageous for convoying situations where a base station is not available or the base station is too far away to remove correlated measurement errors. The DRTK technique is especially useful in low-visibility desert environments during dust

storms where vision-based sensors will fail, but the unobstructed sky provides many visible satellites without multipath interference. The minimum hardware requirements for DRTK are two GPS receivers and antennas, a communication link, and a central processing unit (CPU).

3.1.1 Single-Difference Measurement Models

Similar to carrier-phase DGPS, GPS measurements are differenced to remove correlated errors between GPS receivers in close proximity to improve the estimation of the integer ambiguity in the carrier-phase measurement. The first difference computed is the difference between measurements taken at two GPS receivers. This is known as the *single-difference* measurement, denoted by the Δ preceding the respective measurement's symbols, and is given in (3.1) and (3.2). The geometric representation of the single-difference measurement is shown in Figure 3.1.

$$\Delta\rho^j_{r,b} = ||\mathbf{r}^j_{r,b}|| + cb_{r,b} + \eta^j_{r,b} \tag{3.1}$$

$$\Delta\phi^j_{r,b} = ||\mathbf{r}^j_{r,b}|| + cb_{r,b} + \lambda N^j_{r,b} + \epsilon^j_{r,b} \tag{3.2}$$

Comparing equations (2.1-2.2) and (3.1-3.2), respectively, the atmospheric error terms are effectively removed and the clock error terms are combined in $b_{r,b}$. The combined clock error term is the difference in relative clock errors between the receivers in relation to each SV. The subscript r, b denote *rover* and *base*, respectively. The range term, $||\mathbf{r}^j_{r,b}||$, is now the range between the receivers. $\lambda N^j_{r,b}$ represents the difference in integer ambiguity terms between the rover and base receiver. The respective nondeterministic noise terms on the single-difference pseudorange and carrier-phase measurements are assumed to be independent Gaussian random variables. By differencing or summing independent Gaussian random variables, the variance of the sum is the sum of the variances as shown in (3.3).

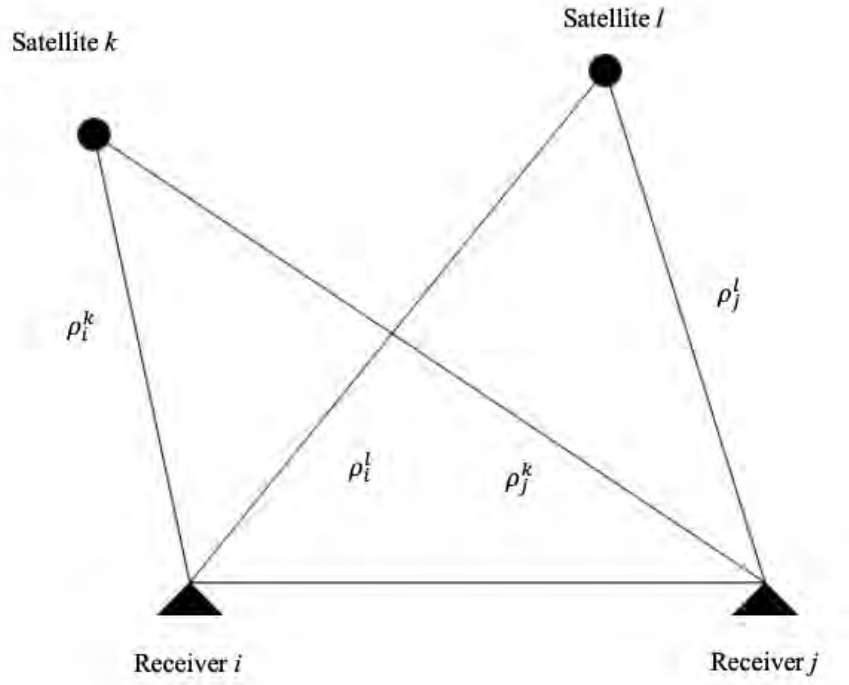

Figure 3.1: Single-difference $\Delta\rho_{i,j}^l = (\rho_i^l - \rho_j^l)$, $\Delta\rho_{i,j}^k = (\rho_i^k - \rho_j^k)$. Two receivers observe pseudoranges from two satellites simultaneously.

$$\text{var}\left(\sum_{i=1}^{n} X_i\right) = \sum_{i=1}^{n} \text{var}\left(X_i\right) \tag{3.3}$$

where $X_1, X_2, ...$ is a sequence of uncorrelated random variables [50]. A depiction of this consequence is depicted in Figure 3.2. This growth in noise is accounted for in the measurement covariance matrix, $\mathbf{R}$, of the Kalman filter in Section 3.1.2.1.

3.1.2 DRTK Algorithm

The DRTK technique requires multiple steps to achieve *cm* level accuracy. The process is described by the following steps:

- Compute *single-difference* observations from the carrier-phase and pseudorange measurements. This step effectively removes the atmospheric biases from the measurements

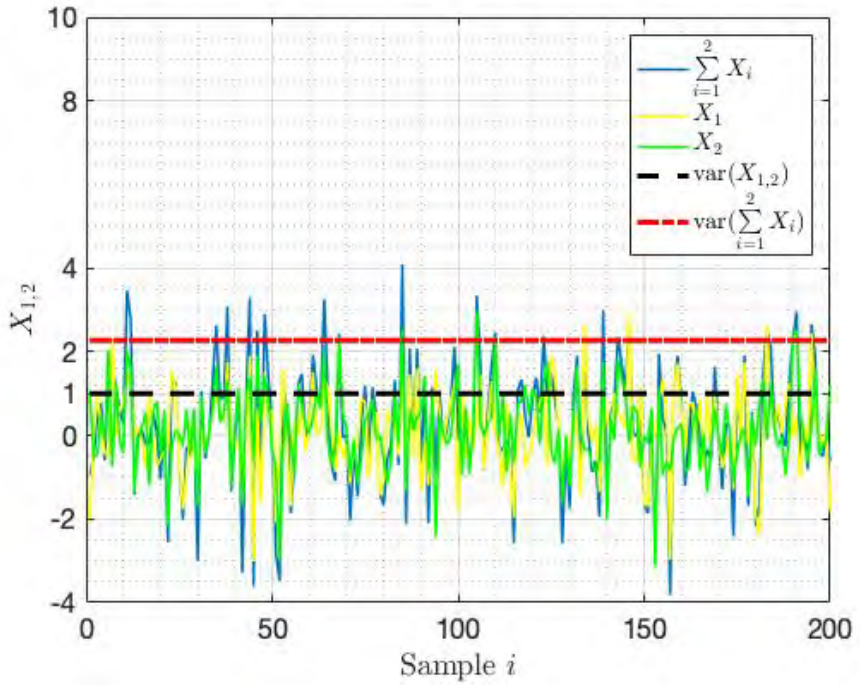

Figure 3.2: The statistical qualities of the sum of two independent Gaussian random variables as given in (3.3).

but leaves the integer ambiguity term on the carrier-phase measurement and the clock bias term on pseudorange and carrier-phase measurements.

- Fuse pseudorange measurements and carrier-phase measurements in a Kalman filter to estimate the relative floating point integer ambiguity term.

- Difference single-difference integer ambiguity estimates and their associated covariance matrix to form *double-difference* estimates that are free of relative clock bias.

- Pass floating point double-difference integer ambiguity estimates and their associated estimated state covariances to the LAMBDA method algorithm to 'fix' the floating point estimates to integers.

- Difference the single-difference carrier-phase measurements and associated unit vectors to form double-difference observations free of relative clock bias.

- Subtract the fixed integer ambiguity estimates from the double-difference carrier-phase measurements and estimate the high-precision relative position vector (HPRPV) with least squares.

3.1.2.1 Kalman Filter Floating Point Ambiguity Resolution

Before beginning discussion of the Kalman filter implemented in this thesis, a brief introduction of the Kalman filter fundamentals is presented. The linear discrete Kalman filter assumes a process to be estimated can be modeled in the form shown in 3.4.

$$\mathbf{x}_{k+1} = \mathbf{\Phi}_k \mathbf{x}_k + \mathbf{w}_k \tag{3.4}$$

The measurement of the process is assumed to occur at discrete points in time in a linear relationship described by 3.5.

$$\mathbf{z}_k = \mathbf{H}_k \mathbf{x}_k + \mathbf{v}_k \tag{3.5}$$

The terms introduced in (3.4) and (3.5) are as follows with m equal to the number of measurements and n equal to the number of states estimated:

- $\mathbf{x}_k$ is a $(n \times 1)$ state vector at time t_k.
- $\mathbf{\Phi}_k$ is a $(n \times n)$ state transition matrix relating $\mathbf{x}_k$ to $\mathbf{x}_{k+1}$ in the absence of a forcing function.
- $\mathbf{w}_k$ is a $(n \times 1)$ vector assumed to be a white sequence with known covariance.
- $\mathbf{z}_k$ is a $(m \times 1)$ vector of measurements at time t_k.
- $\mathbf{H}_k$ is the $(m \times n)$ observation matrix mapping the measurements to the state vector at time t_k.

- $\mathbf{v}_k$ is a $(n \times 1)$ vector assumed to be a white sequence with known covariance and having zero crosscorrelation with the $\mathbf{w}_k$ sequence [51].

The Kalman filter described in this thesis uses single-difference pseudorange and carrier phase measurements to estimate the integer ambiguity terms. Another common approach is to use double-difference observations; however, this approach introduces complexities in implementation. The main issue is described as *satellite handover*. This occurs when the SV chosen as the master SV from which all single-difference measurements are differenced is out of view and another SV must be chosen as the master. After satellite handover, the Kalman filter must be initialized again. Additionally, double-difference observations are noisier as described by the principal detailed in Section 3.1.1. The states estimated in this thesis are the single-difference integer ambiguity terms corresponding to each SV in view on each frequency (i.e. L1 and L2) tracked as described in (3.6).

$$\mathbf{x} = \begin{bmatrix} N^1_{r,bL1} & \dots N^m_{r,bL1} & N^1_{r,bL2} & \dots N^m_{r,bL2} \end{bmatrix}^{\mathbf{T}} \tag{3.6}$$

The state vector, $\mathbf{x}$, is a column vector of dimension $2m$, where m is the number of common SVs tracked on each frequency. This is under the assumption that a dual-frequency receiver is used.

3.1.2.1.1 Measurement Model The Kalman filter requires a measurement equation to fit the form of (3.7). The single-difference measurement models of (3.1) and (3.2) both include a relative range term, $||\mathbf{r}^m_{r,b}||$, and the carrier phase measurement includes the relative integer ambiguity terms, $N^m_{r,b}$. The relative range term is removed from the equation using the leftnull technique first used in [44]. To illustrate this technique, the single difference carrier phase and pseudorange measurement models given in (3.2) and (3.1) are rewritten in matrix form in (3.8).

$$\mathbf{z} = \mathbf{H}\mathbf{x} \tag{3.7}$$

$$\begin{bmatrix} \Delta\rho^j_{r,b} \\ \Delta\phi^j_{r,b} \end{bmatrix} = \begin{bmatrix} a^j_{b_x} & a^j_{b_y} & a^j_{b_z} & 1 \\ a^j_{b_x} & a^j_{b_y} & a^j_{b_z} & 1 \end{bmatrix} \begin{bmatrix} r^j_{r,b_x} \\ r^j_{r,b_y} \\ r^j_{r,b_z} \\ cb_{r,b} \end{bmatrix} + \begin{bmatrix} 0 \\ \lambda \end{bmatrix} N^j_{r,b} \tag{3.8}$$

Note that the respective noise terms on each measurement have been removed for simplicity. The true range between receiver r and receiver b has been decomposed into the direction cosines, $(a^j_{b_x}, a^j_{b_y}, a^j_{b_z})$, of the unit vector pointing from receiver b to the SV j, and the x, y, and z components of the relative position vector (RPV) in the ECEF Cartesian coordinate frame. In this thesis, the matrix in (3.8) containing the direction cosines and the ones corresponding to the relative clock bias term is referred to as the geometry matrix, $\mathbf{G}$. Given that the relative position between the two receivers is less than 20 km, the direction cosines between receiver b and SV j are approximately equal to the direction cosines between receiver r and SV j. This approximation holds because the direction cosines are by definition, the ratio of the difference between the receiver position and satellite position in each dimension to the distance to the j^{th} SV [52]. The distance to the SV is much greater than the difference between the receivers; therefore, it is an acceptable approximation to assume that the direction cosines of each receiver to the SVs are approximately equal. Figure 3.3 illustrates this property.

Estimating the single-difference integer ambiguities, $N^m_{r,b}$, is achieved by isolating them from the range information within the single-difference pseudorange and carrier phase measurements. This operation is accomplished by premultiplying each term in (3.8) by the left nullspace of the geometry matrix, $\mathbf{G}$. The left nullspace of $\mathbf{G}$ is the nullspace of $\mathbf{G^T}$. The useful property of this is by definition, every vector $\mathbf{y}$ in the nullspace of $\mathbf{G^T}$ is perpendicular to every column of $\mathbf{G}$. The result is $\mathbf{G^T y} = \mathbf{0}$. Similarly, $\mathbf{y^T G} = \mathbf{0}$. This is known as the *Fundamental Theorem of Linear Algebra*, Part 2 by Strang in [53]. The left nullspace of the geometry matrix, $\mathbf{G}$, is denoted by $\mathbf{L}$. Multiplying (3.8) by $\mathbf{L}$ eliminates $\mathbf{G}$ and the column

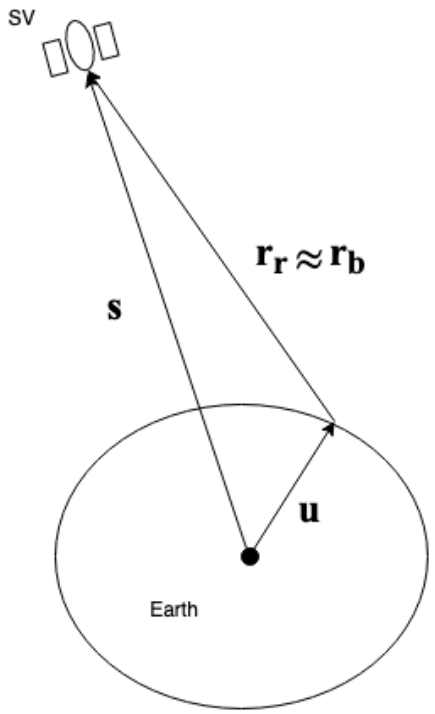

Figure 3.3: Position vector representation, where **s** is the vector computed with Ephemeris data, **u** is the vector describing user position, and **r** is the SV-to-receiver vector.

vector containing the relative range terms and relative clock bias. The measurement vector **z** is now given by 3.9.

$$\mathbf{z} = \mathbf{L}\begin{bmatrix}\Delta\rho_{r,b_{L1}}^{1\ldots m} & \Delta\rho_{r,b_{L2}}^{1\ldots m} & \Delta\phi_{r,b_{L1}}^{1\ldots m} & \phi_{r,b_{L2}}^{1\ldots m}\end{bmatrix}^{\mathbf{T}} \tag{3.9}$$

where **z** is a vector containing common single-difference pseudorange and carrier-phase measurements from SV 1 to m on the L1 and L2 frequencies multiplied by the left nullspace of **G**, **L**.

The measurement noise covariance matrix, **R**, represents the expected measurement error. This stochastic measurement error is assumed to be a white sequence with known covariance structure and having zero crosscorrelation with the process noise, $\mathbf{w_k}$, as described in (3.10). The measurement covariance is calculated at each measurement update using (2.3) and (2.4). Assuming the measurement noise between receivers is uncorrelated, the expected

measurement covariance is the summation of the individual measurement error from each receiver as described in Section 3.1.1. In matrix form, $\mathbf{R}$ is given by example for one SV in (3.11). In actuality, the dimension of $\mathbf{R}$ is twice the number of visible SVs. Additionally, $\mathbf{R}$ is updated using $\mathbf{L}$ as given in (3.12).

$$\mathbf{E}[\mathbf{v_k}\mathbf{v_i}^T] = \begin{cases} \mathbf{R_k}, & \text{if } i = k \\ \mathbf{0}, & \text{if } i \neq k \end{cases} \tag{3.10}$$

$$\mathbf{R} = \begin{bmatrix} \sigma^2_{r_{DLL}} + \sigma^2_{b_{DLL}} & 0 \\ 0 & \sigma^2_{r_{PLL}} + \sigma^2_{b_{PLL}} \end{bmatrix} \tag{3.11}$$

$$\mathbf{R} = \mathbf{L}\mathbf{R}\mathbf{L}^T \tag{3.12}$$

The observation model for the Kalman filter, $\mathbf{H}$, contains rows of zeros relating the single-difference pseudorange measurements to the states, and rows of appropriate carrier wavelengths relating the single-difference carrier-phase measurements to the states. $\mathbf{H}$ is given in 3.13.

$$\mathbf{H} = \mathbf{L}\begin{bmatrix} 0_{2m\times m} & 0_{2m\times m} \\ \lambda_{L1}I_{m\times m} & 0_{m\times m} \\ 0_{m\times m} & \lambda_{L2}I_{m\times m} \end{bmatrix} \tag{3.13}$$

The goal of fitting the Kalman filter form, $\mathbf{z} = \mathbf{H}\mathbf{x}$ has now been completed. The update step of the Kalman filter is given in (3.14-3.16).

$$\mathbf{K}_k = \mathbf{P}^-_k\mathbf{H}^\mathbf{T}_k[\mathbf{H}_k\mathbf{P}^-_k\mathbf{H}^\mathbf{T}_k + \mathbf{R}_k]^{-1} \tag{3.14}$$

$$\mathbf{P}^+_k = [\mathbf{I} - \mathbf{K}_k\mathbf{H}_k]\mathbf{P}^-_k \tag{3.15}$$

$$\hat{\mathbf{x}}^+_\mathbf{k} = \hat{\mathbf{x}}^-_\mathbf{k} + \mathbf{K}_k[\mathbf{z}_k - \mathbf{H}^\mathbf{T}_k\hat{\mathbf{x}}^-_\mathbf{k}] \tag{3.16}$$

3.1.2.1.2 System Model The states estimated are assumed to be constant so long as the receiver does not experience *cycle-slip*. Cycle-slip occurs when there is a discontinuity in a receiver's continuous phase lock on a SV's signal. The assumption of constant integer ambiguities yields a state transition matrix with no dynamics (i.e. identity matrix, $\mathbf{I}$). The state transition matrix, $\mathbf{\Phi}$, is an identity matrix with dimensions equal to the number of single-difference integer ambiguity states. The process noise covariance matrix, $\mathbf{Q}$, is by definition the expected variance of disturbances affecting the system model as given in (3.17). The Kalman filter assumes that this disturbance is a white sequence with known covariance structure as given in (3.17). Theoretically, since the states are constant, the process noise covariance matrix, $\mathbf{Q}$, could be set to zero. However, this would cause the state covariance matrix, $\mathbf{P}$, to approach zero, thus causing the Kalman gain matrix, $\mathbf{K}$, to approach zero. The consequence of this is that the Kalman filter relies upon the system model and does not account for new measurement information. This is commonly known as the filter going to 'sleep'. To mitigate this, an empirically determined fictitious process noise term of 10×10^{-7} is introduced to $\mathbf{Q}$. Therefore, $\mathbf{Q}$ is an identity matrix multiplied by the fictitious process noise. The state estimates and state covariance matrix are propagated with the standard Kalman filter time update equations given in (3.18) and (3.19).

$$\mathbf{E}[\mathbf{w_k}\mathbf{w_i}^T] = \begin{cases} \mathbf{Q_k}, & \text{if } i = k \\ \mathbf{0}, & \text{if } i \neq k \end{cases} \tag{3.17}$$

$$\hat{\mathbf{x}}_\mathbf{k}^- = \mathbf{\Phi_{k-1}}\hat{\mathbf{x}}_\mathbf{k-1}^+ \tag{3.18}$$

$$\mathbf{P}_k^- = \mathbf{\Phi_{k-1}}\mathbf{P}_{k-1}^+\mathbf{\Phi_{k-1}}^\mathbf{T} + \mathbf{Q} \tag{3.19}$$

3.1.2.1.3 Initialization and Implementation The initial state estimates are computed by taking the difference in the single-difference carrier phase and pseudorange measurements and dividing by the carrier wavelength to convert the estimate to units of cycles as shown in (3.20).

$$\hat{\mathbf{x}}_{\mathbf{0}}^{-} = \begin{bmatrix} \left(\Delta\rho^{1}_{r,b_{L1}} - \Delta\phi^{1}_{r,b_{L1}}\right)/\lambda_{L1} \\ \vdots \\ \left(\Delta\rho^{m}_{r,b_{L1}} - \Delta\phi^{m}_{r,b_{L1}}\right)/\lambda_{L1} \\ \\ \left(\Delta\rho^{1}_{r,b_{L2}} - \Delta\phi^{1}_{r,b_{L2}}\right)/\lambda_{L2} \\ \vdots \\ \left(\Delta\rho^{m}_{r,b_{L2}} - \Delta\phi^{m}_{r,b_{L2}}\right)/\lambda_{L2} \end{bmatrix} \tag{3.20}$$

The state covariance matrix, $\mathbf{P}$, is initialized with a value of 0.5, indicating an expected initial estimate error of half a cycle. This result was determined empirically in [25]. Dimensionally, $\mathbf{P}$ is $(2m \times 2m)$.

During operation, two events cause a necessary adjustment of the state vector and state covariance matrix. The most common event is the loss or gain of a visible SV. When this occurs, the state covariance matrix must be reduced to account for a lost SV, and appended with the expected initial error value of 0.5 to account for a newly acquired SV. This operation adds or removes rows and columns associated with the placement of the acquired or lost SV, respectively. In the case of adding a new SV, a column and row of zeros is added to include the new SV; however on the diagonal, the zero is replaced with the expected initial error value of 0.5. Additionally, the state vector is appended with the initial estimate of the integer ambiguity as described in (3.20). Conversely, when an SV is lost, its associated row and column are removed from the state covariance matrix, and its integer ambiguity state is removed from the state vector.

The second event to be accounted for is a cycle-slip as briefly introduced earlier. When this occurs, the integer ambiguity estimate is no longer valid and must be reinitialized with the same routine described for a new SV. The cyle-slip may be reported by the receiver or may be estimated independently by (3.21).

$$dN^j_{k,k-1} = \left[\left(\Delta\rho^j_k - \Delta\phi^j_k\right) - \left(\Delta\rho^j_{k-1} - \Delta\phi^j_{k-1}\right)\right]/\lambda \tag{3.21}$$

If the value of $dN^j_{k,k-1}$ exceeds a threshold of plus or minus one cycle, the measurement is deemed to have experienced a cycle-slip.

3.1.2.2 Double-Difference Operation

At each time step, the state vector and state covariance matrix provided by the Kalman filter undergo the double-difference operation. This transformation is performed to remove the residual relative receiver clock bias errors. First, the SV most directly overhead is selected as the master SV from which to difference all other state estimates, measurements, and state covariances. The SV most directly overhead is chosen because it is least affected by propagation delays from the atmosphere, because it has the shortest path to Earth [17]. The geometric representation of the double-difference measurement is shown in Figure 3.4. This linear operation is performed by a transformation matrix of the form given in (3.22).

$$\mathbf{D} = \begin{bmatrix} 1 & -1 & 0 & 0 & 0 \\ 0 & -1 & 1 & 0 & 0 \\ 0 & -1 & 0 & 1 & 0 \\ 0 & -1 & 0 & 0 & 1 \end{bmatrix} \tag{3.22}$$

In this example, the second SV of five is chosen as the master. After using (3.22) to double-difference $\hat{\mathbf{x}}$, one is left with $(m-1)$ double-difference state estimates. This transformation is performed as follows on the state vector and state covariance matrix.

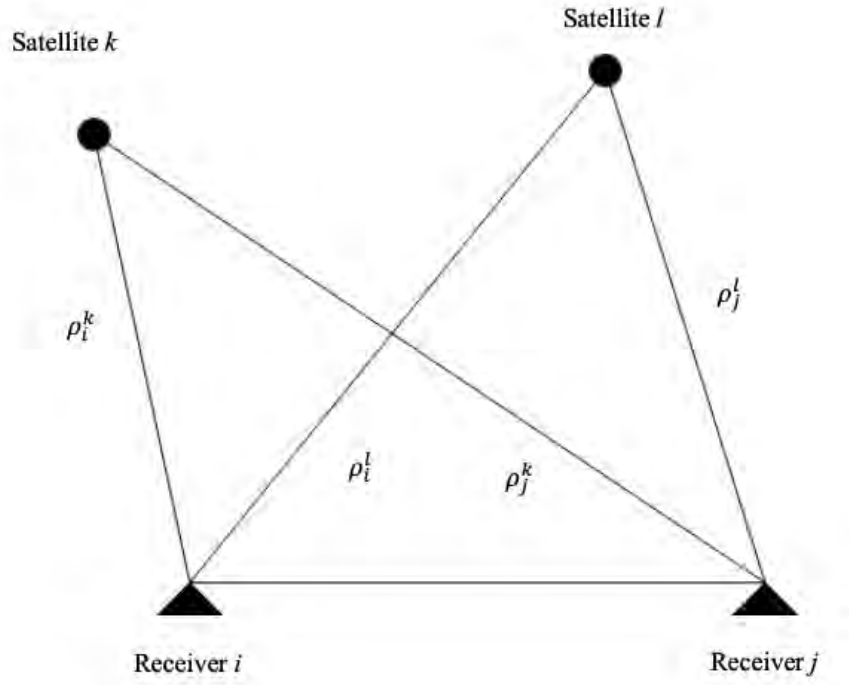

Figure 3.4: Double-difference $\Delta\nabla\phi_{i,j}^{l,k} = (\rho_i^l - \rho_j^l) - (\rho_i^k - \rho_j^k)$. Two receivers observe pseudo-ranges from two satellites simultaneously.

$$\hat{\mathbf{x}}_{\mathbf{DD}} = \mathbf{D}\hat{\mathbf{x}} \tag{3.23}$$

$$\mathbf{P}_{\mathbf{DD}} = \mathbf{DPD}^{\mathbf{T}} \tag{3.24}$$

At each time step, the state vector containing the double-difference integer ambiguity estimates, $\hat{\mathbf{x}}_{\mathbf{DD}}$, and their associated state covariance matrix, $\mathbf{P}_{\mathbf{DD}}$, are passed along to the Least-squares Ambiguity Decorrelation Adjustment (LAMBDA) algorithm to aid in fixing the float estimates of $N_{r,b}^j$ to integers.

3.1.2.3 LAMBDA Method for Integer Fixing

The obvious approach to fixing the float estimates to integers would be to simply round the float estimates of $N_{r,b}^j$ up or down to integers; however, the float estimates of $N_{r,b}^j$ are

correlated. Simple rounding does not take advantage of all the information available. The LAMBDA method was developed by Peter Teunissen between 1993 and 1996 to address this issue. Its MATLAB implementation was clearly described by de Jonge & Tiberius and is freely available online today. The LAMBDA method takes into account both the variance and covariance of each floating point integer ambiguity estimate. The algorithm can be broken down into the following steps:

- refine the search space by decorrelating the estimates through a transformation,
- perform a sequential conditional least-squares based search [54].

The LAMBDA method provides the most likely set of integer ambiguities; however, they are not guaranteed to be correct. A common metric to determine if the set of integer ambiguity estimates is correct is known as the ratio test [55]. Two candidate sets of double-difference integer ambiguities and their deviation from the original floating point estimates transformed to double-difference are determined by LAMBDA. If the ratio of deviations exceeds a certain threshold, the most likely candidate set of integer ambiguities is deemed correct; otherwise, no fixed integer solution is available. The threshold value used in this thesis is three, based on the results in [56]. According to Borre & Strang in [57], a common commercial software for RTK by Ashtech uses a threshold of (1.2-1.4) with satisfactory results. If fixed integers are available, the relative position solution is known as the high precision relative position vector (HPRPV) or the *fixed* solution; if not, the float solution is used and is known as the low-precision relative position vector (LPRPV) or the *float* solution. A good resource for a thorough description of LAMBDA is presented in [57]. The LAMBDA ratio result will be described by λ_R in this thesis.

3.1.2.4 Least Squares Relative Position Vector Estimation

The prior work presented thus far in this chapter is to determine the best estimate of the double-difference integer ambiguity estimates. The final step in determining an RPV is

to use least squares with the best integer ambiguity estimates available (i.e. float or fixed). The solution procedure is the same regardless of the quality of the estimates. The RPV estimate problem takes the form of 3.25.

$$\Delta\nabla\phi_{r,b} - \lambda\Delta\nabla N_{r,b} = \Delta\vec{a}_b\vec{r}_{r,b} + \epsilon \tag{3.25}$$

where SV notation has been removed for brevity. The nabla and delta pair, $\Delta\nabla$, signifies that the carrier phase measurements have been double-differenced with the same technique described in (3.23). Additionally, the preceding Δ before the unit vector $\vec{a}_b$ signifies that the unit vector has undergone differencing from the master SV to form the correct geometry. The RPV is then estimated with the least squares solution given in (3.26).

$$\vec{r}_{r,b} = \left(\Delta\vec{a}_b^{\mathbf{T}}\Delta\vec{a}_b\right)^{-1}\Delta\vec{a}_b^{\mathbf{T}}\left(\Delta\nabla\phi_{r,b} - \lambda\Delta\nabla N_{r,b}\right) \tag{3.26}$$

3.2 Experimentation and Results

3.2.1 Experimentation

To verify this technique, dynamic data was taken with two NovAtel receivers and two NovAtel pinwheel antennas fixed in an attitude baseline configuration atop the GAVLAB's Lincoln Mkz (see Figure 3.5). The Mkz was driven around the Auburn University campus while an embedded software implementation of DRTK in C++ calculated the RPV between the two antennas in real time. The path taken is shown in Figure 3.6. GPS data was logged at 1 Hz. This experimental setup was implemented for ease of verification of the algorithm, because the baseline could be hand measured and verified with RTK to ensure the solution was accurate. The RTK solution was provided by NovAtel's GrafNav RTK post-processing software. Since the baseline magnitude is constant, the rms of the baseline magnitude provided by RTK, which was 1.90 m, was used for comparison. The base station

Figure 3.5: The GAVLAB's Lincoln Mkz used for data collection and algorithm verification.

chosen for RTK correction was the ALA1 Continuously Operating Reference Station (CORS) located near Auburn University's campus.

3.2.2 Results

The results of this brief experiment are tabulated in Table 3.1. The rms error is misleading, but is the expected result. DRTK is similar in principal to the RTK post-processing software used to determine truth for comparison. DRTK and RTK have correlated errors that are removed when differencing the two solutions. This result implies that DRTK achieves performance similar to that of RTK, which is 2 cm [58] (see Figure 3.10). Throughout the whole data run, which was 10 min, the DRTK fixed solution was available 82% of the time. The periods that the fixed solution was lost was when driving under trees near Jordan-Hare stadium and in urban canyons within Auburn University's campus (see Figure 3.7-3.8). In Figure 3.9, the LAMBDA ratio results are included to compare with the solution. An increasing LAMBDA ratio indicates increased confidence in the solution. The LAMBDA ratio threshold used was 3. Near sample 250, the LAMBDA ratio dipped under the threshold, so

Figure 3.6: Total path of experiment.

the fixed solution was deemed incorrect. The initial fix occurred after two time steps, which is a TTFF of two epochs or two seconds.

Table 3.1: Statistics on High-Precision and Low-Precision DRTK Baseline Errors

Solution Type	RMSE (cm)	Var (cm^2)
Fixed	0.32	0.10
Float	33.3	1086

3.3 Conclusions

In conclusion, DRTK has been shown to provide RTK level relative positioning solutions with one caveat. A DRTK solution will not be available as often as an RTK solution. DRTK necessitates common measurements between two receivers just as RTK, but RTK always has

Figure 3.7: Portion of experiment when DRTK solution was lost under foliage and obstruction by Jordan-Hare stadium.

one unobstructed receiver. For example, if two vehicles in a leader-follower formation are traveling along and must drive through a tunnel, a DRTK RPV solution will be available only when both vehicles are outside of the tunnel. With RTK, a solution will be available to each vehicle as long as the vehicle has common SVs in view. However, DRTK is a marked improvement to standalone positioning as described in Chapter 2, and is the best option available for GPS based relative positioning when there is no base station or network RTK service available.

The results shown in Table 3.1 are in agreement with previous treatments of this subject in [46, 47, 58, 59]. The contents of this chapter are the foundation for the rest of this thesis. Chapter 4 will introduce a similar DRTK technique that includes *a priori* baseline information as a constraint. Chapter 5 will then use the technique developed in Chapter 4 with the DRTK technique in this chapter in a cascaded Kalman filter framework to aid in integer ambiguity resolution when using single-frequency receivers.

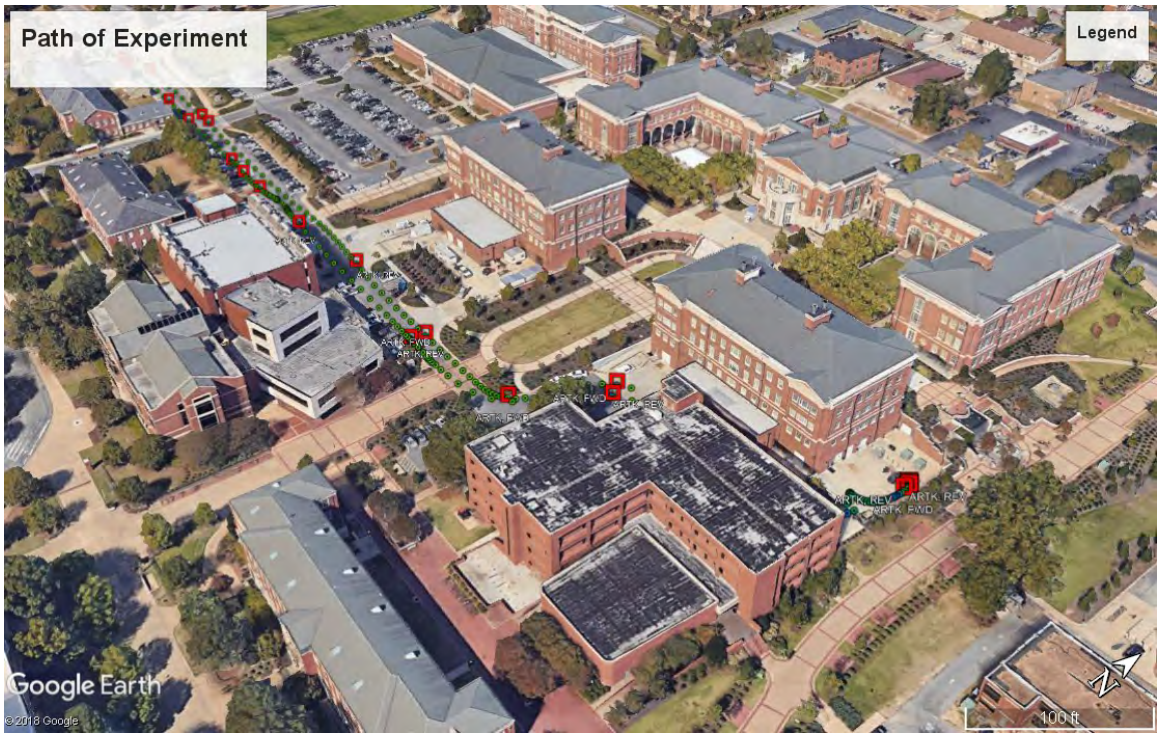

Figure 3.8: Portion of experiment when DRTK solution was lost within an urban canyon.

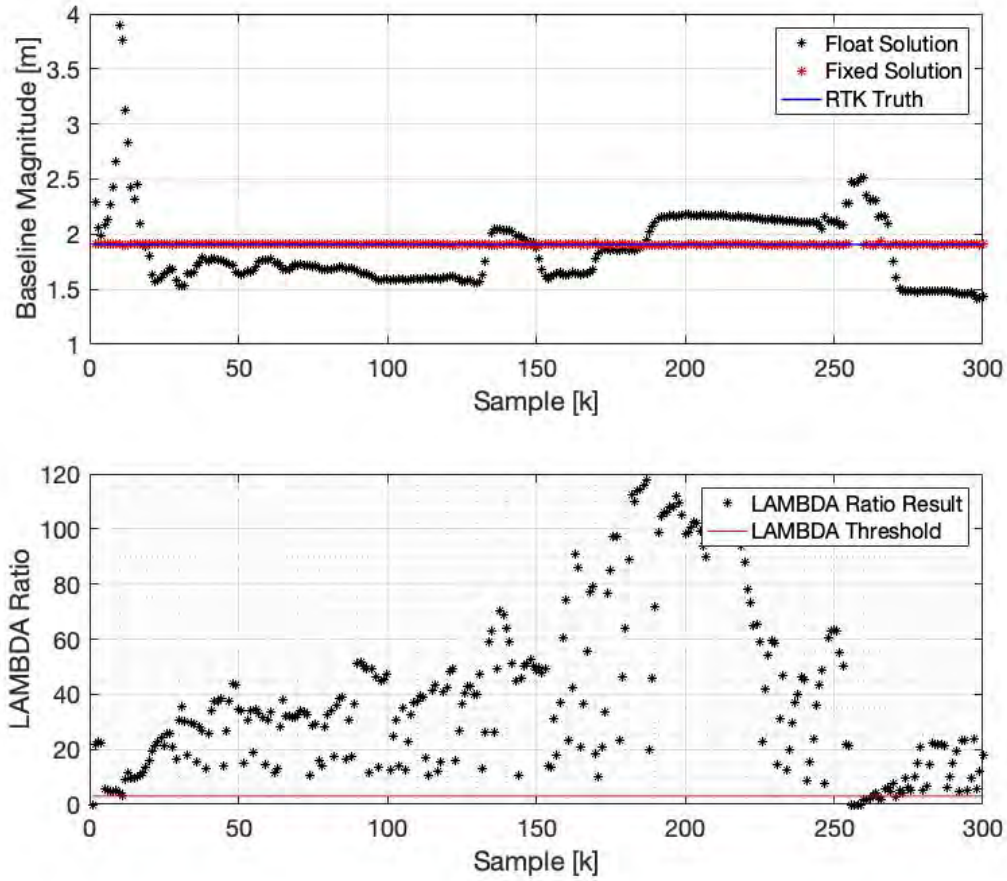

Figure 3.9: Comparison of DRTK solution with LAMBDA ratio result.

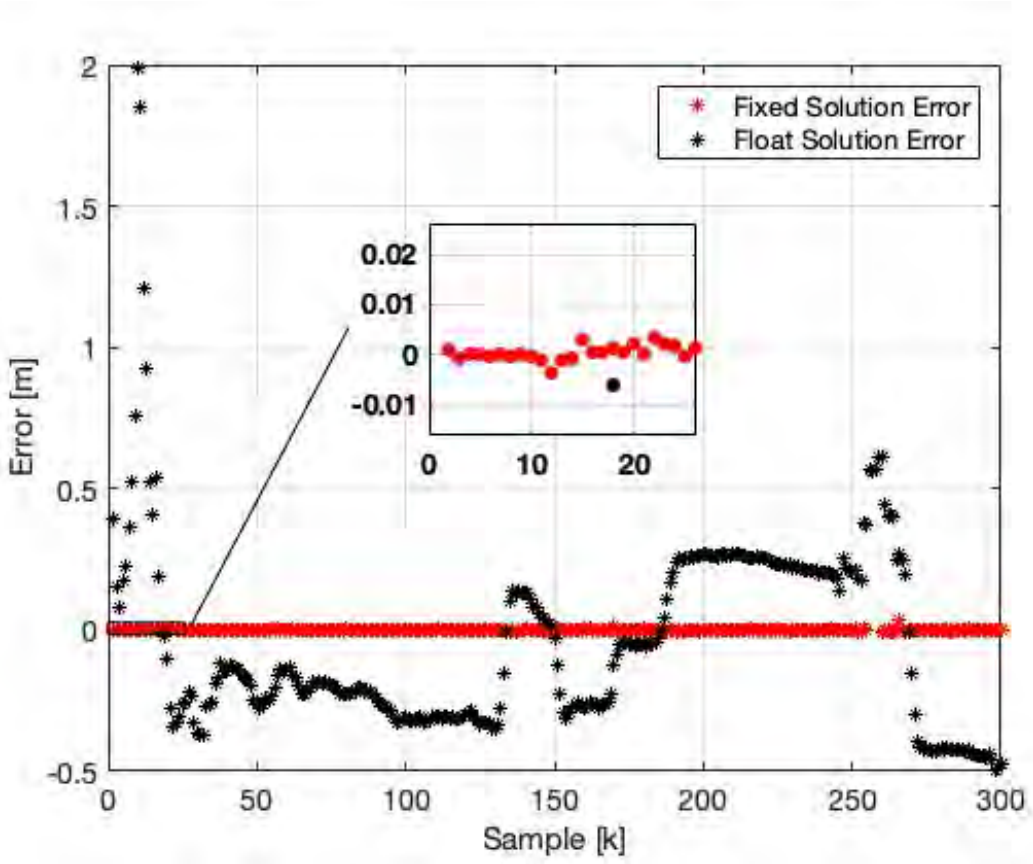

Figure 3.10: Error in the DRTK baseline magnitude estimation.

Chapter 4

Fixed Attitude Configuration of Antennas

When two antennas are fixed in a baseline attitude configuration on a vehicle, the baseline magnitude is constant and known with a high degree of certainty when measured with RTK [60]. This *a priori* baseline magnitude information may be leveraged to constrain the possible positions of the auxiliary antenna to a virtual sphere with radius equal to the baseline magnitude. The first treatment of this technique was done by Cohen in [17, 61]. A description of this relationship is depicted in Figure 4.1. The initial interest in this relationship was in the application of spacecraft attitude determination; however, it is also useful for determining valuable information for deriving additional measurements for relative positioning between vehicles when necessitated by poor receiver quality.

4.1 Applying the Baseline Magnitude Constraint

Similar to the DRTK technique, a Kalman filter is used to estimate the floating point relative integer ambiguity terms between the two antennas. The main difference is that this estimator must include relative range terms in the state vector to apply the baseline magnitude constraint. The same measurements are used as well as the same assumptions about the process dynamics of the integer ambiguity states. The inclusion of the relative range terms in the state vector necessitate modeling of expected receiver and clock bias dynamics. The state vector for this filter is introduced in (4.1) with new subscripts a, b introduced to represent the auxiliary and base antenna, respectively.

$$\mathbf{x} = \begin{bmatrix} x_{a,b} & y_{a,b} & z_{a,b} & cb_{a,b} & c\dot{b}_{a,b} & N^1_{r,b} \dots N^m_{r,b} \end{bmatrix}^{\mathbf{T}} \tag{4.1}$$

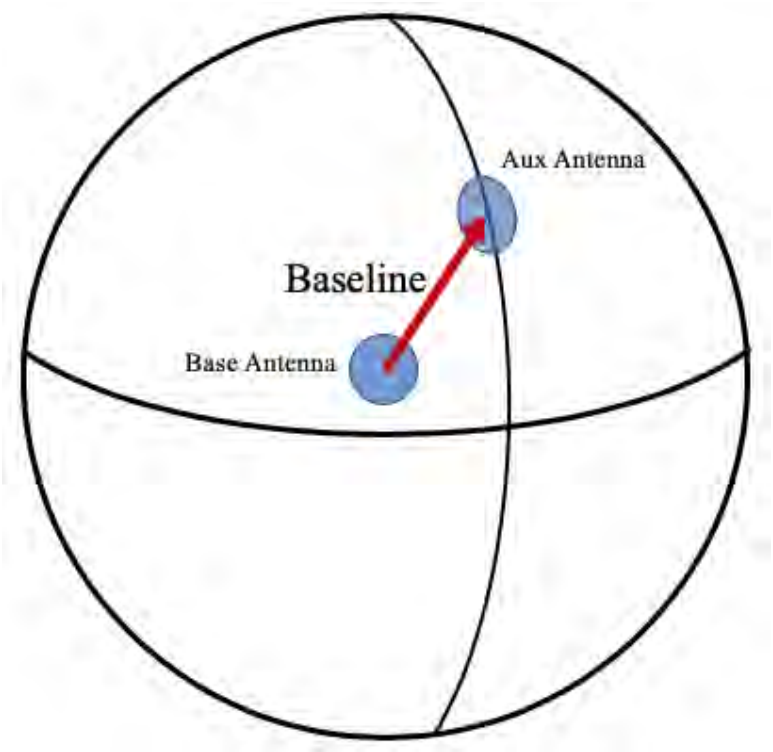

Figure 4.1: Baseline magnitude constraint.

The notation used now is similar as before, but no attempt is made to differentiate between measurement signal frequencies for brevity. The superscript m represents the total number of common measurements between receivers regardless of frequency.

The baseline measurement model is equal to the norm of the relative position vector between the two fixed antennas. The model used is simply shown by,

$$\beta = \sqrt{x_{a,b}^2 + y_{a,b}^2 + z_{a,b}^2} \tag{4.2}$$

where β represents the baseline magnitude. This baseline magnitude is determined via RTK or a simple hand measurement with a tape measure. With RTK, the magnitude is known to a couple of mm. For this thesis, the *a priori* baseline magnitude was determined using RTK. If RTK was not available, the hand measurement could be used with an expected error of a couple of cm, because the actual phase center of the antenna where measurements are made is not necessarily the geometric center of the antenna and must be approximated [5].

4.2 Fixed Attitude-Baseline DRTK

In essence, the technique presented here is similar to DRTK. There is no static base station and both receivers are dynamic. The key difference is the inclusion of *a priori* baseline magnitude information as a constraint. To differentiate this technique from DRTK, it will be referred to as *Fixed Attitude-Baseline DRTK* (FAD) for the remainder of discussion.

4.2.1 Measurement Model

The measurements used are the same as those used for DRTK with the addition of the *a priori* baseline magnitude measurement, $\hat{\beta}$. The measurement vector is given in (4.3).

$$\mathbf{z} = \begin{bmatrix} \Delta\rho_{a,b}^{1\ldots m} \\ \Delta\phi_{a,b}^{1\ldots m} \\ \hat{\beta} \end{bmatrix} \tag{4.3}$$

To account for the baseline magnitude measurement, the geometry matrix given in (3.8) is altered. The last row of the observation matrix, $\mathbf{H}$, is linearized by differentiating the measurement model in (4.2) with respect to the state vector in (4.3), which results in a unit vector pointing from the auxiliary antenna to the base antenna. This newly constructed observation matrix is given in (4.4).

$$\mathbf{H} = \begin{bmatrix} a_{b_x}^j & a_{b_y}^j & a_{b_z}^j & 1 & 0 & 0_{m\times m} \\ a_{b_x}^j & a_{b_y}^j & a_{b_z}^j & 1 & 0 & \lambda I_{m\times m} \\ \frac{x_{a,b}}{\beta} & \frac{y_{a,b}}{\beta} & \frac{z_{a,b}}{\beta} & 0 & 0 & 0_{1\times m} \end{bmatrix} \tag{4.4}$$

The measurement noise covariance matrix introduced in (3.11) is appended with the expected error associated with the baseline magnitude measurement to account for the additional measurement. This is known as *constrained Kalman filtering*. An RTK derived measurement of the baseline has an expected variance of 0.1 cm^2. This can be seen as a tunable parameter. In theory, setting this variance to zero would introduce a hard constraint;

however this was determined to be undesirable because the carrier phase and pseudorange measurements were devalued so much as to ignore their information. Additionally, setting the measurement noise covariance of the baseline magnitude measurement may also introduce numerical instability [62]. The Kalman filter is in essence a recursive Bayesian filter that operates on the law of total probability, so the noisier measurements are weighted lower and essentially ignored if the variance for the baseline measurement is set too low [63]. The measurement noise covariance matrix in (4.5) is identical to the one introduced in (3.11) with the addition of the expected baseline magnitude measurement error. For this work, the best results were found when inflating the baseline measurement error to $0.7^2\ cm^2$.

$$\mathbf{R} = \begin{bmatrix} \sigma^2_{a_{DLL}} + \sigma^2_{b_{DLL}} & 0 & 0 \\ 0 & \sigma^2_{a_{PLL}} + \sigma^2_{b_{PLL}} & 0 \\ 0 & 0 & \sigma_\beta \end{bmatrix} \tag{4.5}$$

4.2.2 System Model

The assumptions for the process noise, Q_N, of the integer ambiguity states remains the same as introduced in Chapter 3. The expected process noise of the relative baseline $x_{a,b}, y_{a,b}, z_{a,b}$ terms is expected to be low for a ground vehicle when compared to that of an aircraft, especially since the two antennas are fixed to the same body in motion. This is treated as a tunable parameter to achieve desired performance. These terms are represented by $Q_{x,y,z}$ in (4.8). Finally, the state transition matrix is altered to account for the additional states in (4.9).

4.2.2.1 Receiver Clock Process Model

To properly estimate the clock process dynamics, two states are required: clock bias, b, and drift, $\dot{b}$. These states represent the phase and frequency errors in the atomic frequency standard or crystal oscillator in the receiver [17]. This two state model represents the expectation that both the frequency and phase of the oscillator will experience a random walk

over a short period of time. Therefore, the process model for the clock is commonly modeled as given in (4.6). The clock's process noise is represented by $\mathbf{w_c}$. The state transition matrix for this two state clock model is given in (4.7). $\mathbf{Q_b}$ is multiplied by two in (4.8) because the stochastic components of each receiver clock are assumed to be uncorrelated. If the two receivers don't share clocks with the same model parameters, the process model in (4.6) may be performed separately and summed in (4.8).

$$\mathbf{Q_b} = \mathbf{E}[\mathbf{w_c}\mathbf{w_c}^T] = \begin{bmatrix} S_f\Delta t + S_g\frac{\Delta t^3}{3} & S_g\frac{\Delta t^2}{2} \\ S_g\frac{\Delta t^2}{2} & S_g\Delta t \end{bmatrix} \tag{4.6}$$

$$\mathbf{\Phi_c} = \begin{bmatrix} 1 & \Delta t \\ 0 & 1 \end{bmatrix} \tag{4.7}$$

The white noise spectral amplitudes S_b and S_f can be related to the classical Allan variance parameters. The approximate relation given by Brown & Hwang in [51] is $S_f = h_0/2$ and $S_g = 2\pi^2 h_{-2}$. The coefficients needed for these approximations are given in Table 4.1. Note that the coefficents given in Table 4.1 correspond to clock error in units of seconds; therefore, they must be multiplied by the squared speed of light $(3 \times 10^8)^2$.

Table 4.1: Typical Power Spectral Density Coefficients for Various Timing Standards

Timing Standard	h_0	h_{-2}
Compensated Crystal	$2(10^{-19})$	$2(10^{-20})$
Ovenized Crystal	$8(10^{-20})$	$4(10^{-23})$
Rubidium	$2(10^{-20})$	$4(10^{-29})$

$$\mathbf{Q} = \begin{bmatrix} Q_{x,y,z}I_{3\times3} & 0_{3\times2} & 0_{3\times m} \\ 0_{2\times3} & 2\mathbf{Q_b} & 0_{2\times m} \\ 0_{m\times3} & 0_{m\times2} & Q_N I_{m\times m} \end{bmatrix} \tag{4.8}$$

$$\mathbf{\Phi} = \begin{bmatrix} I_{3\times3} & 0_{3\times2} & 0_{3\times m} \\ 0_{2\times3} & \mathbf{\Phi_c} & 0_{2\times m} \\ 0_{m\times3} & 0_{m\times2} & I_{m\times m} \end{bmatrix} \tag{4.9}$$

4.2.3 Initialization and Implementation

The initial integer ambiguity state estimates are computed the same way as conventional DRTK with (3.20). The initial estimates of relative position are derived from differencing the two receiver's reported standalone position solution. The initial clock bias and clock drift estimates were initialized with values given in [17]. Another approach would be to use each receiver's reported clock bias estimate and then difference the two, but this was not explored. The state covariance matrix terms relating to the baseline components and clock are initialized using the error budget given in [17]. Lastly, the same value of one half cycle is used for initialization of the single-difference integer ambiguity states as presented in Chapter 3.

The same procedures discussed in Section 3.1.2.1 are followed when a cycle-slip occurs. This baseline estimator, like DRTK, produces floating point estimates of single-difference integer ambiguities. Following the same routine, these estimates and associated state covariances are double-differenced and passed to the LAMBDA method for decorrelation and integer fixing. It is important to note that since the state vector does not possess integer ambiguity estimates exclusively, only the portion of the state covariance matrix associated with integer ambiguity estimates is passed to LAMBDA. As an illustration, a matrix with random numbers is presented in (4.10). In this example matrix, only the red portion of the matrix is double-differenced to be passed to LAMBDA. This represents a scenario where four integer ambuigities are estimated, however unrealistic. After the best integer ambiguity estimates are determined, whether they are float or fixed solutions, the same least squares equation in (3.26) is used to estimate the RPV.

$$\mathbf{P_d} = \begin{bmatrix} 1 & 2 & 3 & 3 & 8 & 3 & 4 & 5 & 5 \\ 3 & 55 & 2 & 4 & 6 & 5 & 5 & 6 & 5 \\ 23 & 47 & 74 & 5 & 65 & 7 & 5 & 4 & 5 \\ 42 & 61 & 3 & 5 & 7 & 21 & 2 & 45 & 8 \\ 67 & 1 & 2 & 3 & 4 & 6 & 234 & 7 & 83 \\ 54 & 44 & 2 & 24 & 3 & 24 & 5 & 2 & 3 \\ 78 & 11 & 3 & 33 & 27 & 42 & 3 & 3 & 3 \\ 54 & 4 & 25 & 5 & 3 & 47 & 2 & 2 & 45 \\ 3 & 5 & 5 & 7 & 75 & 36 & 87 & 4 & 56 \end{bmatrix} \tag{4.10}$$

4.3 Experimentation and Results

Verification and analysis of this technique was performed both in simulation and experimentally. The simulations were performed primarily to ensure that the TTFF was improved by including *a priori* baseline magnitude information as a constraint. Experimental data was taken to observe the effects on the LAMBDA ratio results, TTFF, and to validate the simulated results.

4.3.1 Simulation

The simulations were performed in MATLAB. The first step in generating the simulated data was calculating SV positions using broadcast Ephemeris data uploaded to the Crustal Dynamics Data System (CDDIS) website maintained by the National Aeronautics and Space Administration (NASA). Next, arbitrary locations in Auburn, AL were chosen to form a baseline of $\approx 8\ m$. Given locations on Earth and SV positions, dual-frequency pseudorange and carrier phase measurements were generated at 10 Hz by determining the range between the SVs and the simulated receiver locations, and adding biases and normally distributed random noise according to the error budget for GPS given in [17]. The stochastic nature

of the filters necessitated a Monte Carlo simulation to analyze performance [50, 51]. For the simulation, 1,000 separate data sets were generated to compare the FAD and DRTK techniques.

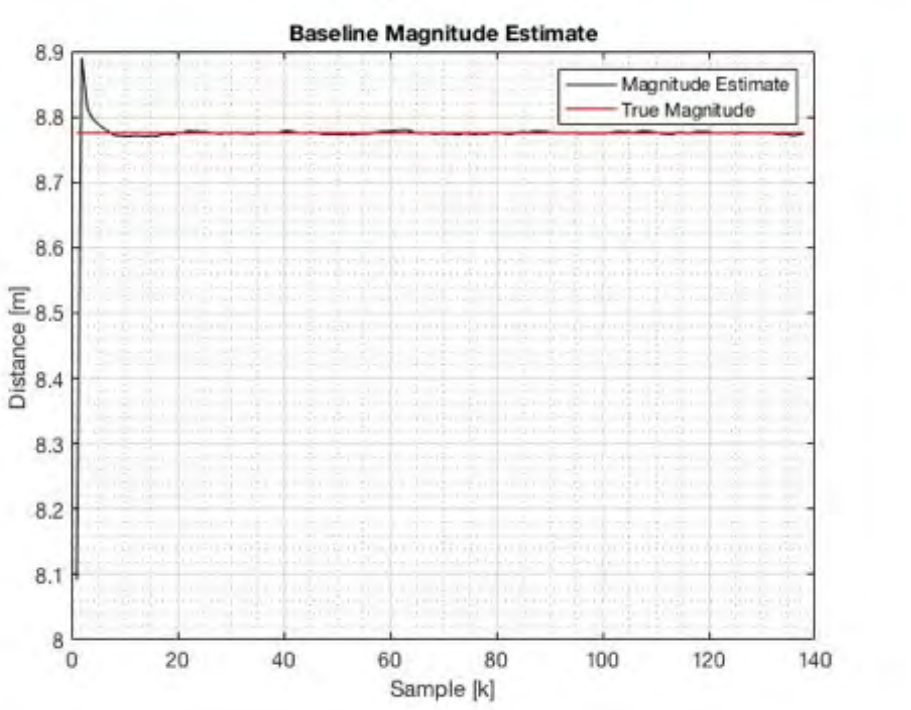

Figure 4.2: FAD converging to the correct baseline magnitude in simulation.

4.3.1.1 Results

The TTFF was determined by simply recording the epoch at which the integer ambiguity estimates equaled the arbitrary integer ambiguities used to construct the carrier phase measurements. The mean TTFF was shown to improve by a factor of 1.4 using FAD. The median TTFF showed an even greater improvement by a factor of 2.65. Lastly, the standard deviation statistics suggest that the TTFF using FAD are more tightly clustered than DRTK, which implies predictability. The summary of statistics from the simulation are given in Table 4.2.

A histogram of the TTFF results is given in Figure 4.4. Comparing FAD with DRTK, it can be seen that the maximum TTFF is greater with DRTK as well as the occurrences

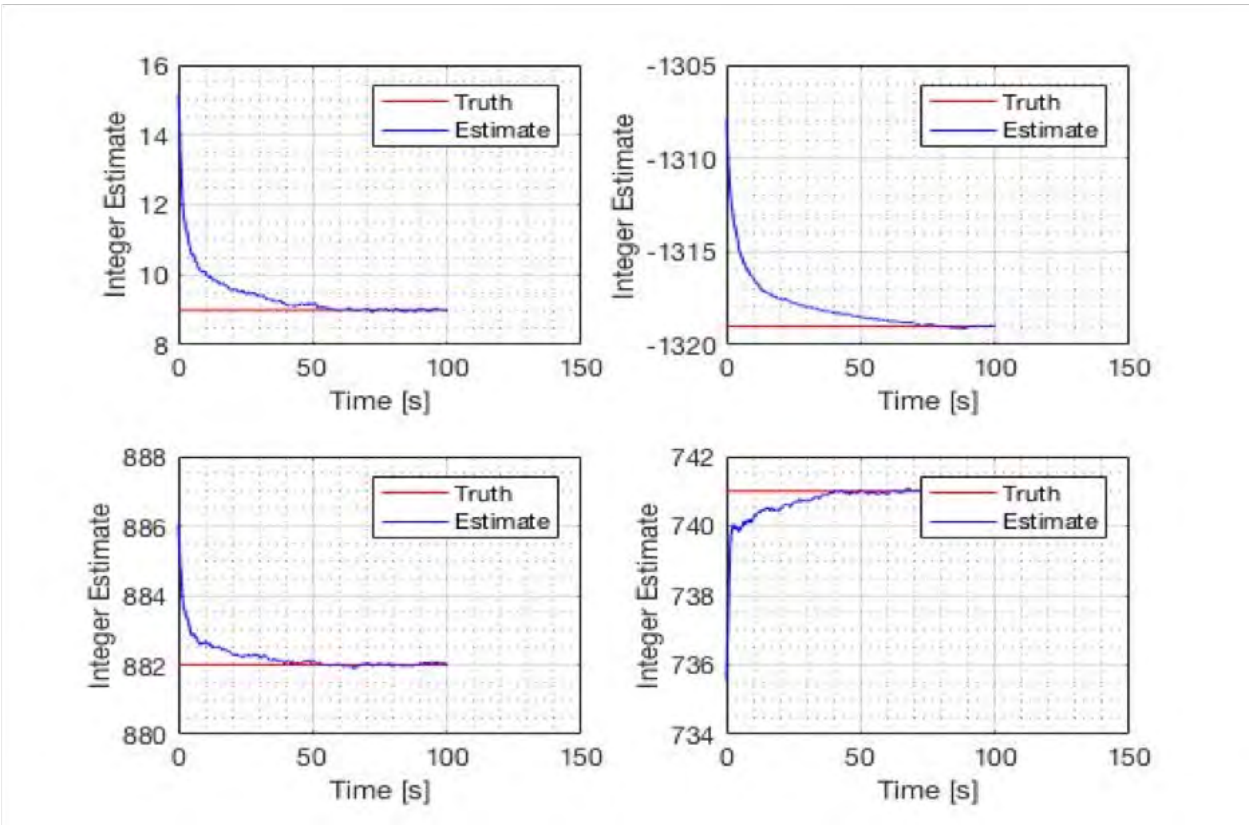

Figure 4.3: Float estimates of four single-difference integer ambiguities converging to simulated values.

of TTFF values greater than 4 s. The histogram shows a right-skewed distribution for both methods; however, the majority of the FAD TTFF values are between 0.5 and 1.5 s, while the DRTK TTFF values are between 1 and 3.5 s as Table 4.2 suggests. The norm of the relative position state estimates and four of the integer ambiguity estimates are shown in Figure 4.1-4.3.

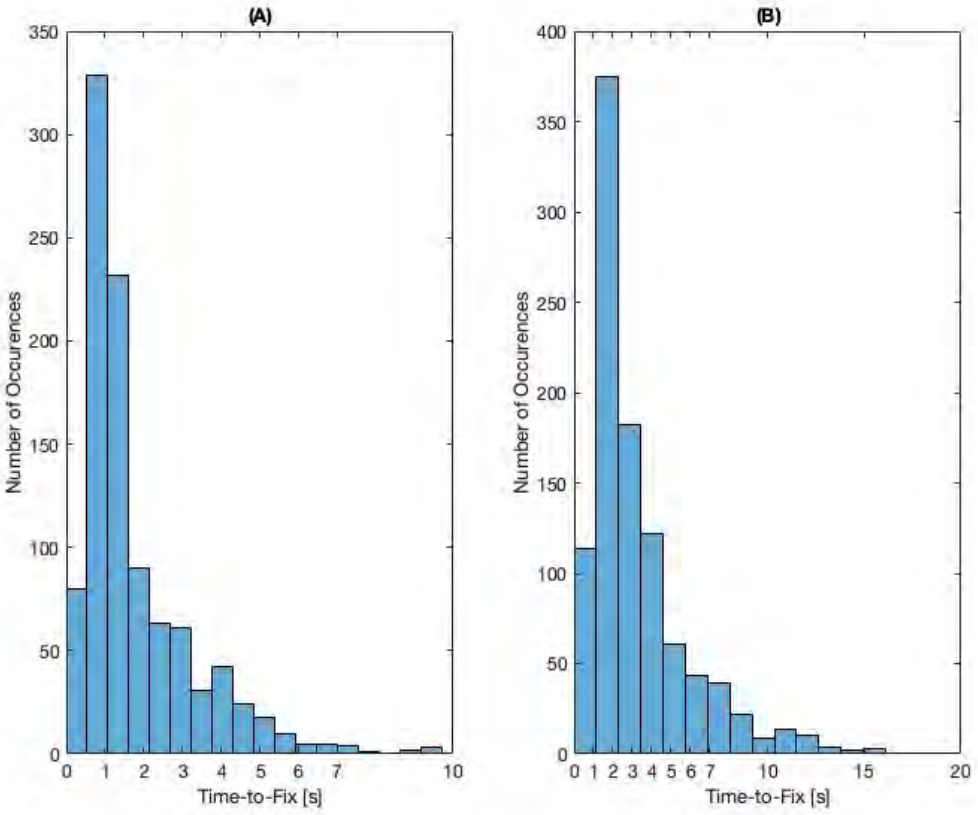

Figure 4.4: TTFF to correct integers with simulated GPS data after 1,000 simulations: (A) FAD, (B) DRTK.

Table 4.2: Statistics on Simulated TTFF with FAD and DRTK

Method	μ (s)	$\tilde{t}$ (s)	σ (s)
DRTK	2.40	3.30	2.60
FAD	1.75	1.25	1.40

4.3.2 Experimentation

Data was collected by two dual-frequency NovAtel OEM4 ProPak receivers with NovAtel pinwheel antennas configured in a fixed attitude baseline configuration atop the GAVLAB

Figure 4.5: Portion of experiment chosen for open sky testing.

Lincoln Mkz as previously shown in Figure 3.5. Raw GPS measurements were collected at 1 Hz and post-processed with NovAtel's GrafNav software for RTK truth. The area selected for open-sky testing can be seen in Figure 4.5. The separation difference between the base station and the rover receiver's effect on DGPS performance has been discussed throughout this thesis. Data was collected around Auburn University's campus to take advantage of the ALA1 CORS base station. The separation distance between the vehicle and the base station as shown in Figure 4.6 remained less than 2 km throughout the experiment. The number of SVs in view over the experiment are given in Figure 4.7. Both the DRTK and FAD algorithms were implemented in MATLAB for comparison. The LAMBDA ratio results and TTFF statistics were generated by reinitializing the filter at 100 different epochs in the data.

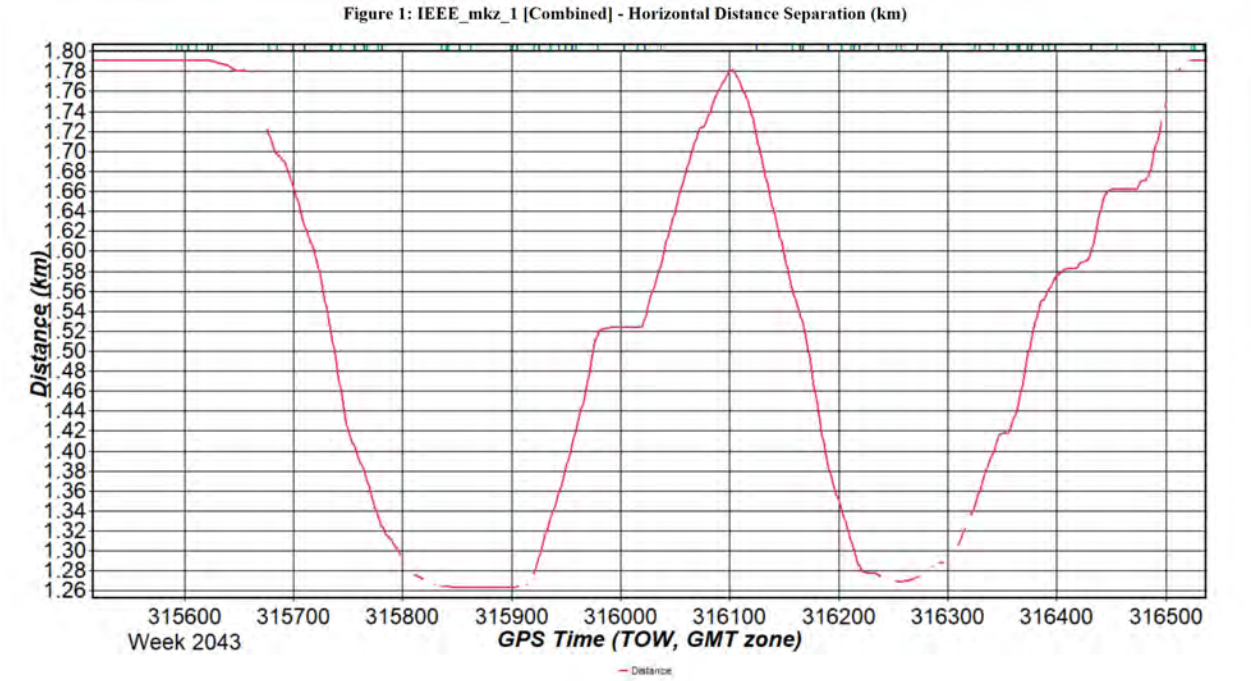

Figure 4.6: Separation distance between the Lincoln Mkz and the base station used for RTK corrections.

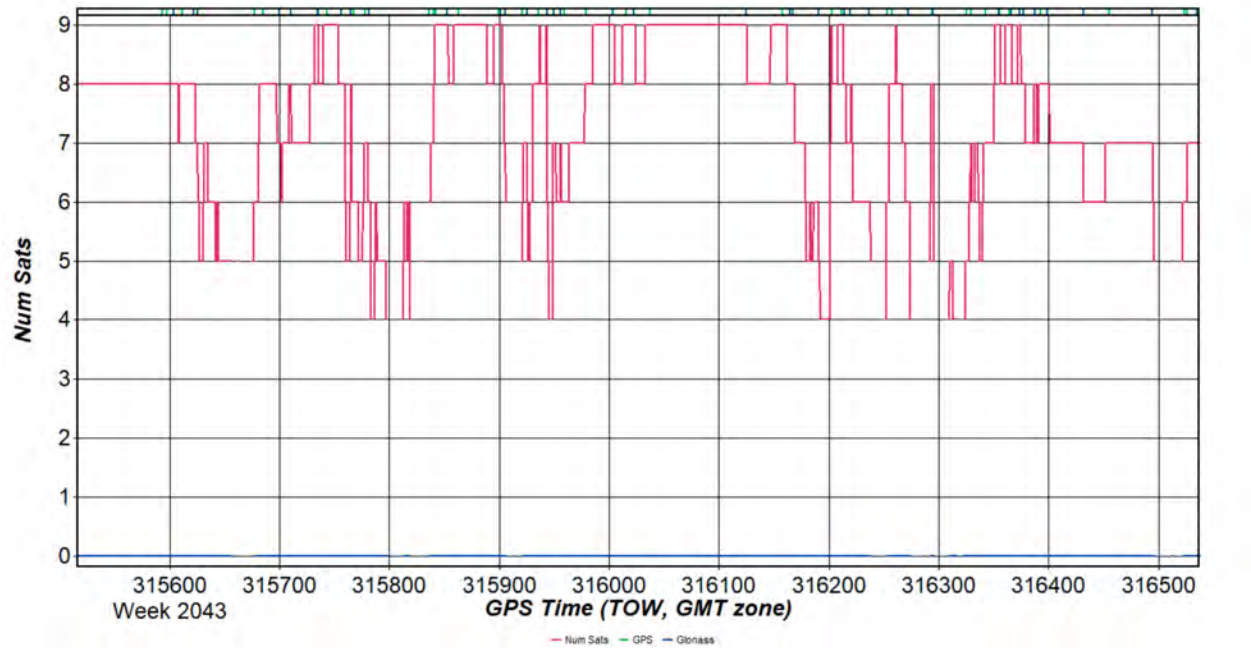

Figure 4.7: Number of SVs in view of the base receiver on-board the Lincoln Mkz.

Table 4.3: Statistics on LAMBDA Ratio Passing Rate

Method	**% Pass on 1^{st} Epoch**	**% Pass on 2^{nd} Epoch**	**% Pass on 3^{rd} Epoch**
DRTK	53	90	100
FAD	87	97	100

4.3.2.1 Results

As expected, once the correct integer ambiguities are determined, both techniques provide practically the same solution. The comparisons of note are TTFF and the LAMBDA ratio result. The simulated results indicated that the FAD technique converges to the correct solution earlier than DRTK. The experimental results not only validated this, but outperformed the simulations. The experimental results are better because the receivers use a technique known as *carrier-smoothing* to reduce the measurement error of the pseudorange measurement by a couple of m [21]. This technique actually violates the assumption of uncorrelated measurements for the Kalman filter but in practice provides better results. The simulation generated *raw* pseudorange with greater variance, which makes resolving the integer ambiguities more difficult.

4.3.2.1.1 LAMBDA and TTFF A summary of the LAMBDA ratio passing rate are given in Table 4.3. Theses statistics represent the TTFF because the integer ambiguities are unknown unless verified through comparison of solutions to the known fixed baseline. Martin suggested the use of the known baseline to detect incorrect integer fixes in [60]. The same technique is applied here to verify correct integer fixing. The experiment showed that both DRTK and FAD achieved correct fixes within three epochs; however, FAD achieved the correct fix on the first epoch 87% of time compared with 53% for DRTK. The gap between ratio passage narrows when comparing passage rates over two epochs and is completely eliminated over three epochs.

The next metric for comparison is the actual value of the LAMBDA ratio over each epoch. FAD consistently provides a higher LAMBDA ratio result over DRTK. This indicates

Table 4.4: Statistics on LAMBDA Ratio Results

Method	**Median λ_R on 1^{st} Epoch**	**Max λ_R on 1^{st} Epoch**	**Min λ_R on 1^{st} Epoch**
DRTK	3.24	15.51	1.70
FAD	4.49	22.50	2.03

a more confident solution. The LAMBDA ratio results over a single portion of data plotted against sample epochs is given in Figure 4.8.

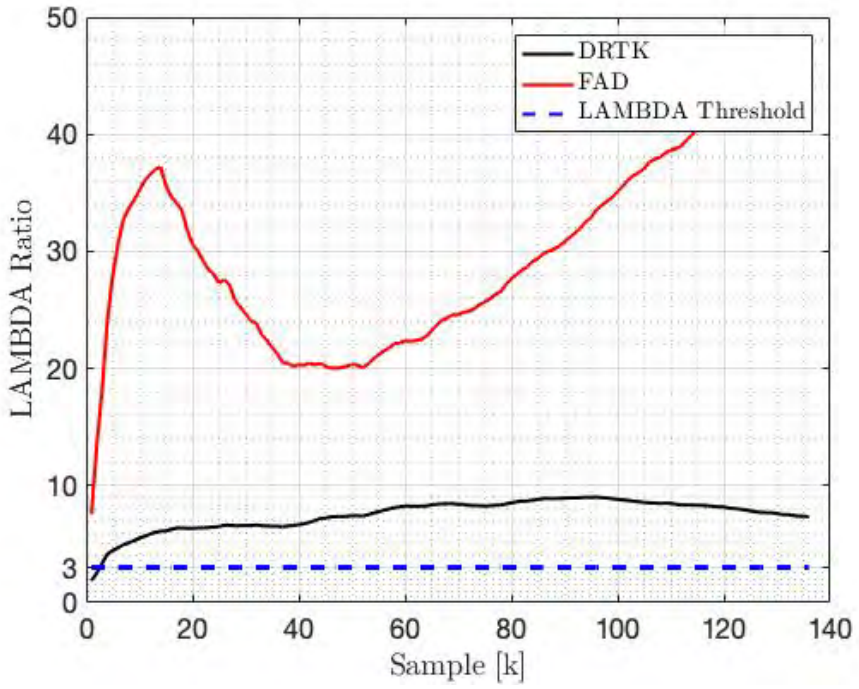

Figure 4.8: Comparison of the LAMBDA ratio results reported by DRTK and FAD over each epoch.

4.3.2.1.2 Uncertainty in the Baseline Magnitude Measurement The uncertainty of the baseline magnitude measurement, $\hat{\beta}$, represented by the choice of σ_β in (4.5) is crucial to integer ambiguity resolution. Figure 4.9 shows the effects of varying the choice of σ_β on λ_R. If σ_β is chosen too low (e.g. $< 0.5\ cm$), FAD struggles to resolve the integer ambiguities because this causes the Kalman filter to devalue the single-difference carrier-phase and single-difference pseudorange measurements. If σ_β is chosen too high (e.g. $> 1.5\ cm$), FAD begins to behave more like conventional DRTK without *a priori* baseline magnitude information.

Tuning σ_β correctly yields a higher initial λ_R that progressively increases over each epoch, which results in a faster TTFF and overall confidence in solution, respectively.

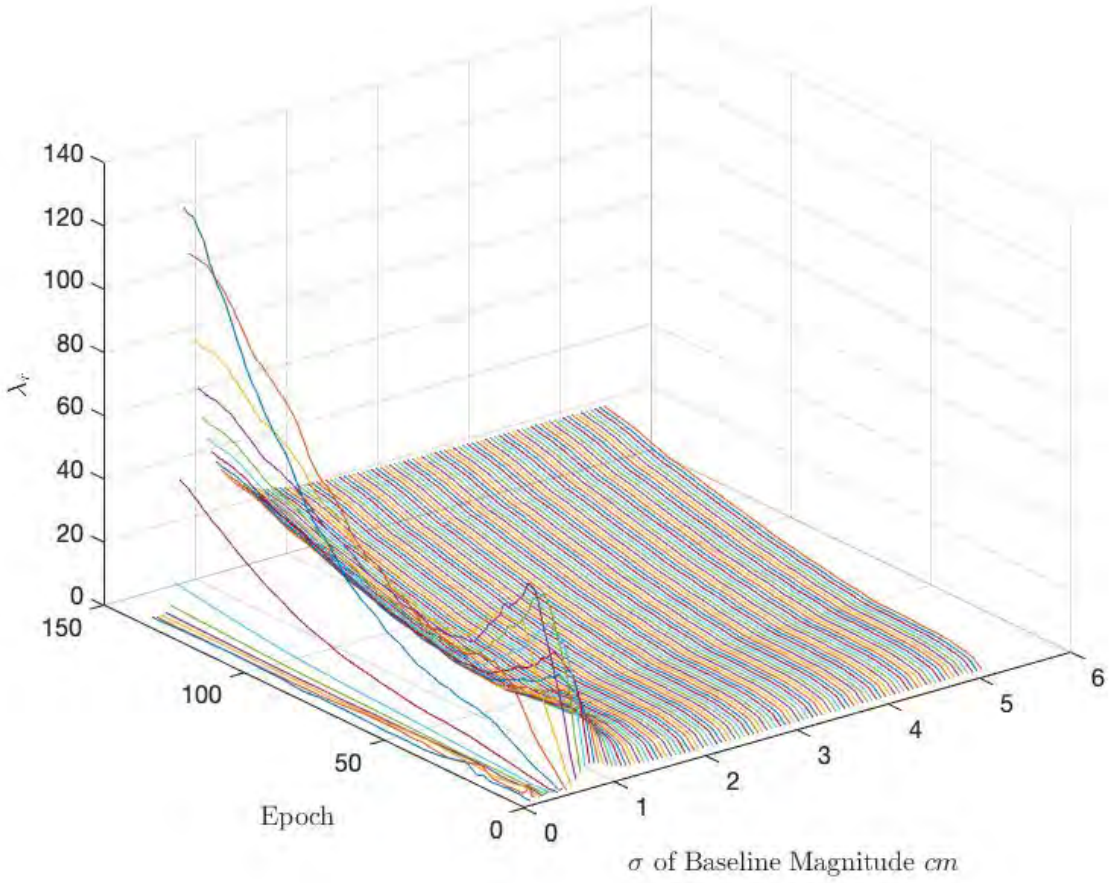

Figure 4.9: The progression of the LAMBDA ratio, λ_r, over varying choices of baseline magnitude measurement accuracy.

4.3.2.1.3 Unaccounted Bias in the Baseline Magnitude Measurement If the baseline magnitude measurement, $\hat{\beta}$, is incorrect (i.e. biased), FAD performance is severely degraded as this unaccounted bias grows. Figure 4.10 illustrates this consequence. The level portions of the plot show correct integer fixing determined by comparing the solution of the HPRPV to the known baseline magnitude. Once the bias in $\hat{\beta}$ increases past $\approx 57\ cm$, FAD begins to provide solutions that do not pass the λ_R threshold of three. The unaccounted

bias in $\hat{\beta}$ degrades FAD so much as to provide much poorer performance than DRTK, which concludes that an accurate $\hat{\beta}$ is crucial for the performance of FAD.

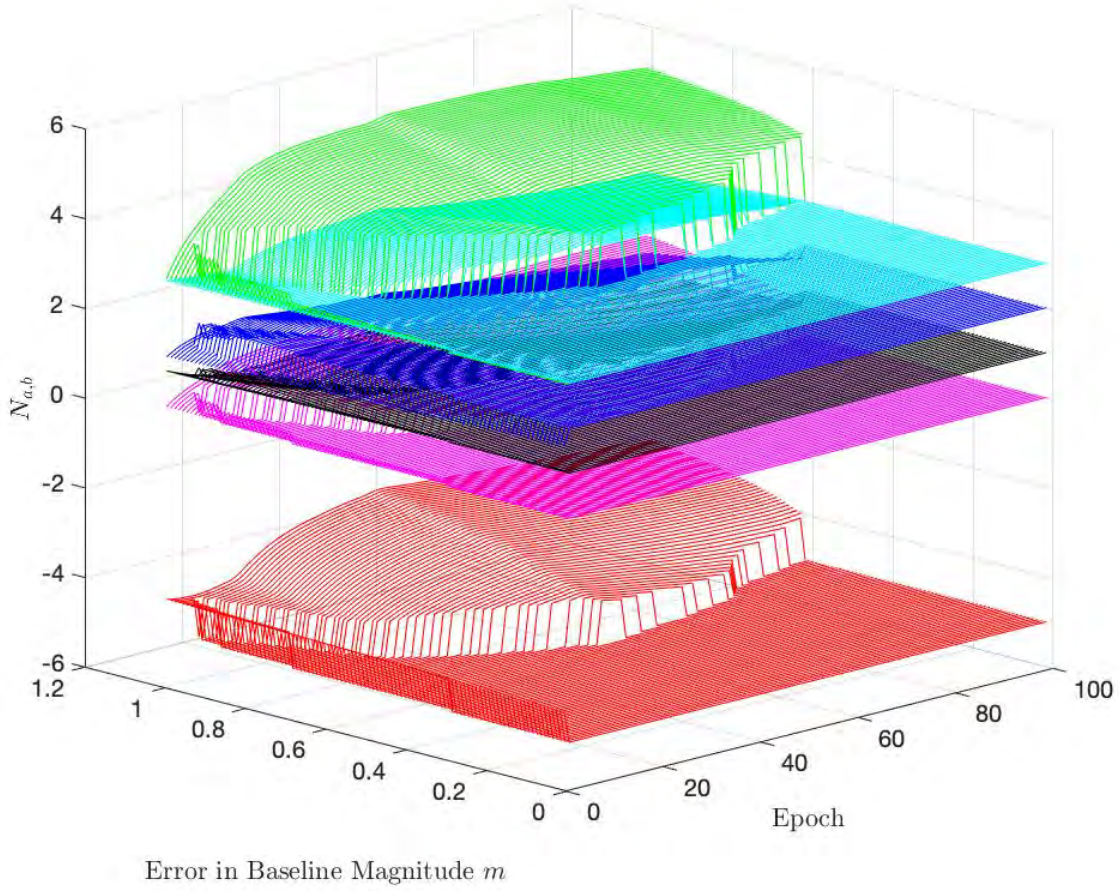

Figure 4.10: The influence of bias in the baseline magnitude measurement on the estimation of the relative integer ambiguities, $N^m_{a,b}$.

4.3.2.1.4 Error Analysis The main goal of including the *a priori* baseline magnitude as a measurement is to provide better initial float solutions, which in turn, provide faster fixed integer ambiguity estimates [60, 61]. The float solution dynamics are given in Figure 4.11. The initial float estimates are better initially with FAD, but then converge to similar solutions. This is expected, because as time progresses, both filters converge to the correct integer ambiguities (see Figure 4.3).

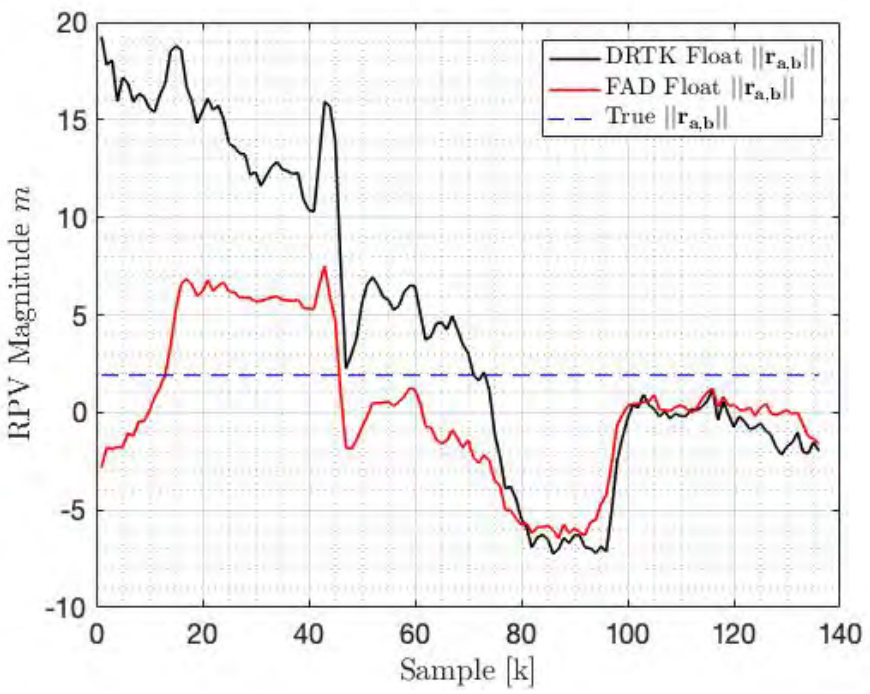

Figure 4.11: Comparison of the DRTK and FAD float solutions.

Figure 4.12 and Figure 4.13 give the best RPV solutions available, and error for both techniques, respectively. It can be seen that both filters not only estimate the correct baseline magnitude (see Figure 4.14 and Figure 4.15), but also each individual component of the RPV. FAD converges to the correct integer ambiguities on the first epoch, while DRTK converges soon after. Once converged, both techniques provide essentially the same results because both are dependent on the accuracy of the carrier-phase measurement. A summary of statistics on the float and fixed RPV magnitude errors is given in Table 4.5, which is in agreement with previous analyses in [25, 46, 47, 58, 59].

Table 4.5: Statistics on Float and Fixed RPV Magnitude Errors

	Float		**Fixed**	
Method	RMSE (cm)	Var (cm^2)	RMSE (cm)	Var (cm^2)
DRTK	9.21	62.85	0.45	0.07
FAD	3.76	14.14	0.46	0.07

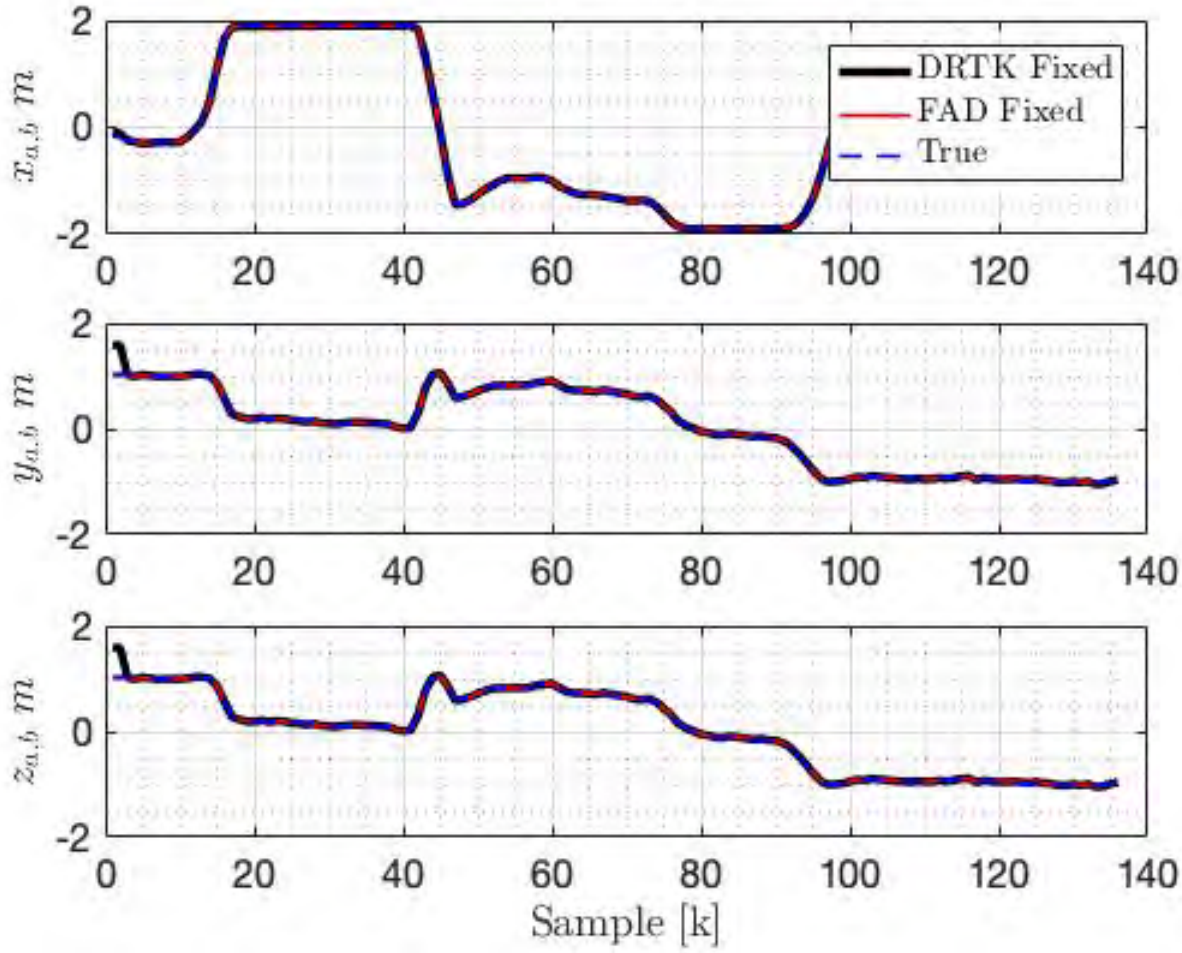

Figure 4.12: Comparison of the fixed DRTK and FAD RPV solutions.

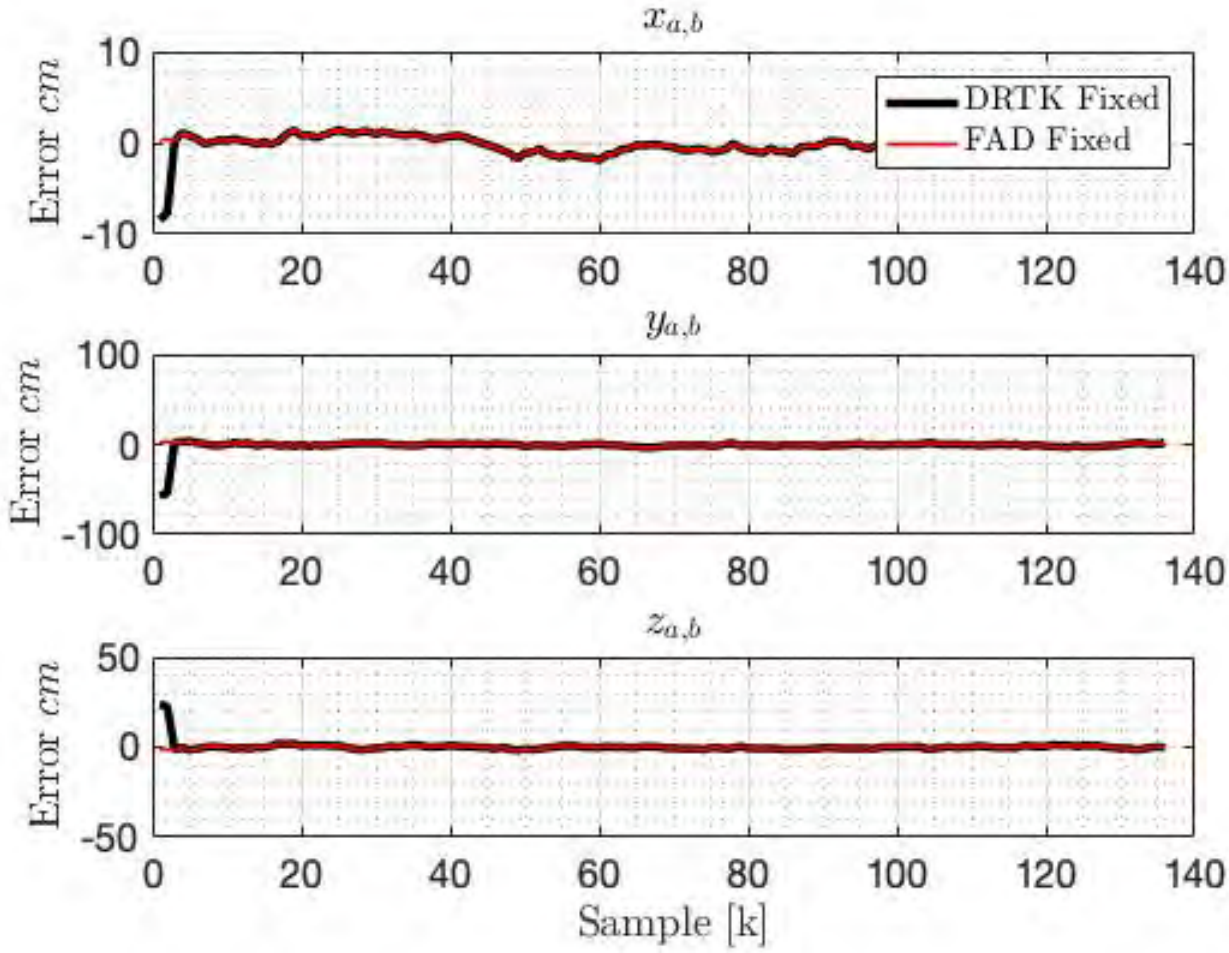

Figure 4.13: Comparison of the error in the fixed DRTK and FAD RPV solutions.

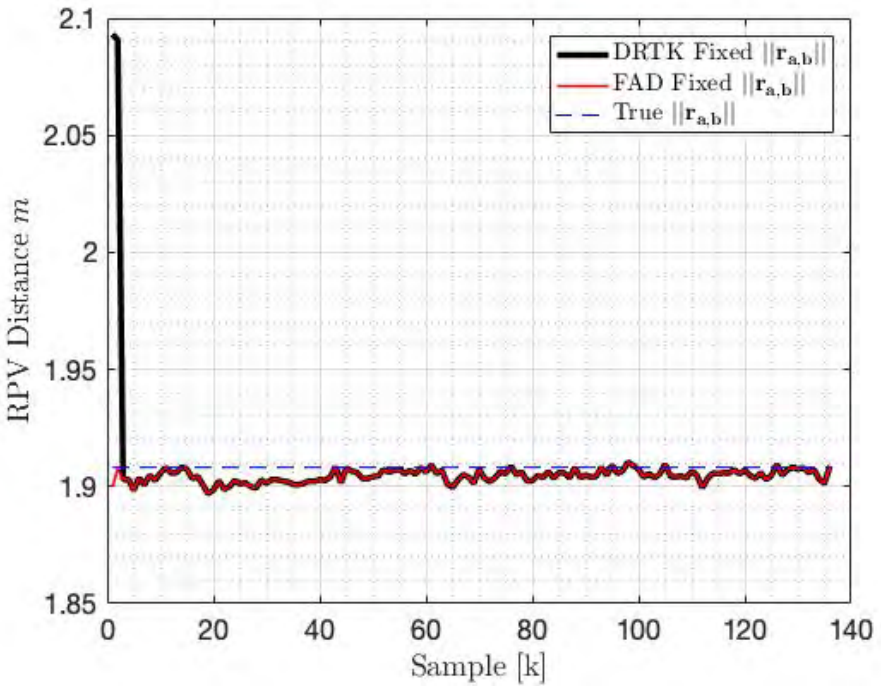

Figure 4.14: Comparison of the DRTK and FAD magnitude solutions.

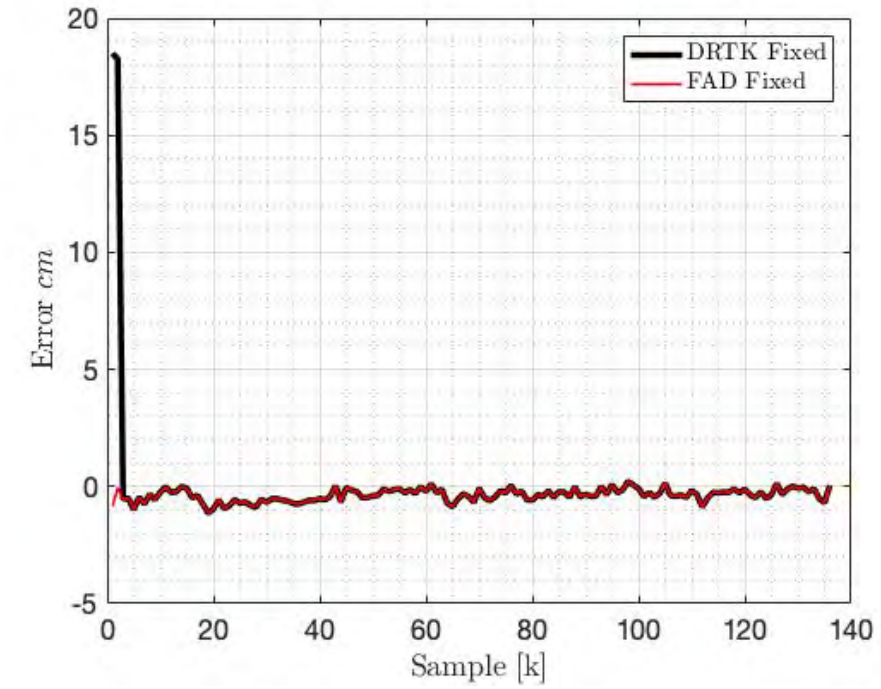

Figure 4.15: Comparison of the error in DRTK and FAD magnitude solutions.

4.4 Conclusions

In summary, the FAD technique outperforms DRTK with regard to TTFF and LAMBDA ratio results. Both techniques, once converged, provide the same HPRPV solution. It is important to note that FAD depends on *a priori* baseline magnitude information that will be unavailable when the antennas are not fixed in relation to one another. FAD's application is especially suited for attitude determination, but is also useful for providing estimates of relative integer ambiguities, relative clock bias, and an RPV that may be used to derive additional measurements between antennas on moving platforms via vector addition that will be discussed in Chapter 5.

Chapter 5

Low-Cost Implementation of FAD with DRTK

The use of low-cost single-frequency receivers has generated much interest in the automotive vehicle industry. The cost sensitivity of the automotive industry requires low-cost hardware without sacrificing safety and performance [64]. Single-frequency receivers differ from dual-frequency receivers in the number of measurements available. Most importantly, atmospheric corrections of the dispersive ionosphere are unavailable for standalone positioning when only a signal frequency is available. Additionally, the L2 frequency is higher than L1; therefore it is less impeded by the atmosphere. The main consequence of less measurements is that the TTFF using DGPS techniques is severely degraded [65].

Using the FAD technique described in Chapter 4 combined with the DRTK technique described in Chapter 3 improves the TTFF and LAMBDA ratio results when compared with DRTK alone by effectively doubling the number of measurements using a cascaded Kalman filter architecture. This development of this technique by Tabb et al. was shown to improve the performance of integer ambiguity resolution when using dual-frequency GPS receivers [66]. It is important to note that this violates the Kalman filter assumption of uncorrelated measurements and is known as the *cascaded Kalman filter problem* [51]. Treatments of this subject may be found in [62, 63, 67]. The work presented here ignores this violation at the consequence of optimality.

5.1 Additional Measurements Derivation

5.1.1 Hardware Configuration

The hardware configuration required for this technique is described in vector form in Figure 5.2 and as an example on Auburn University trucks in Figure 5.1. It should be noted

that the trucks in Figure 5.1 are not actually outfitted with this hardware configuration but were simply used for demonstration. A minimum of three GPS receivers and antennas with a communication link between vehicles is required to achieve this technique. Additionally, two of the receivers must be configured in a fixed attitude baseline with *a priori* baseline magnitude information. The FAD algorithm accepts measurements from the base and auxiliary receivers to determine relative integer ambiguity terms, relative clock bias, and an RPV. These estimates are given to the DRTK algorithm along with measurements from all three receivers to derive additional measurements via vector addition. For the remainder of this discussion, this technique will be described as FAD+DRTK. A diagram of the architecture is given in Figure 5.3.

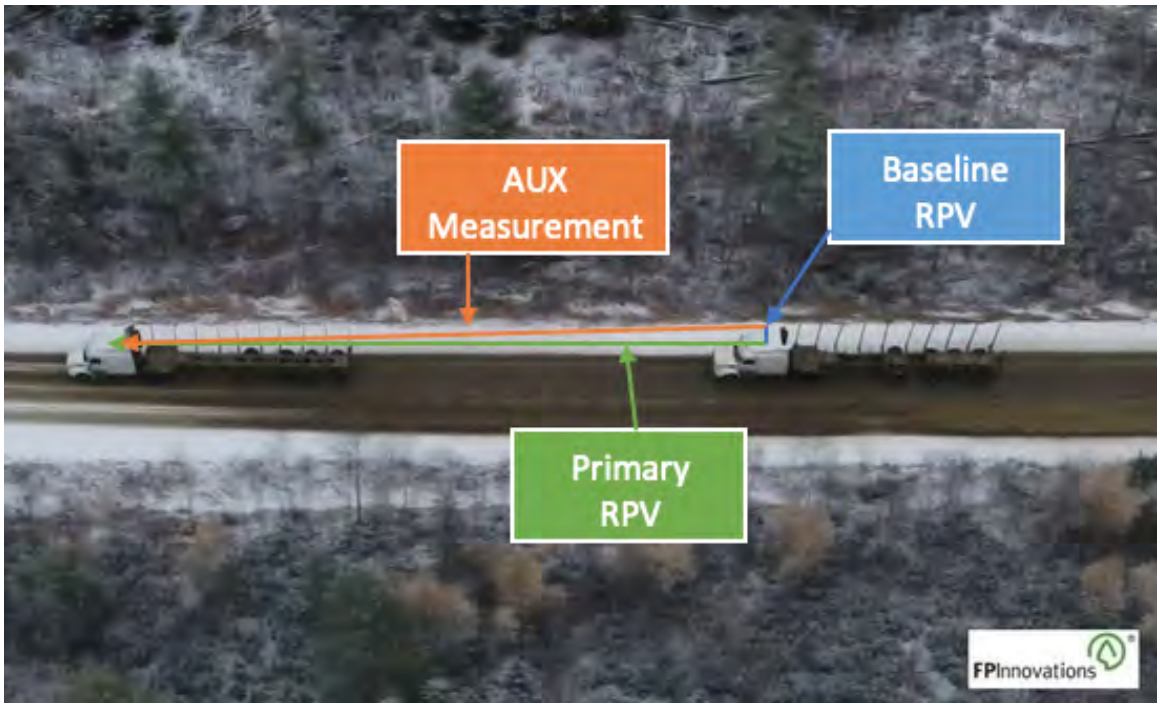

Figure 5.1: Representation of hardware configuration on Auburn University trucks.

5.1.2 Derivation

The measurements used in FAD+DRTK are single-difference pseudorange and carrier-phase . The derivation of the additional measurements is given in (5.1-5.8) with subscripts

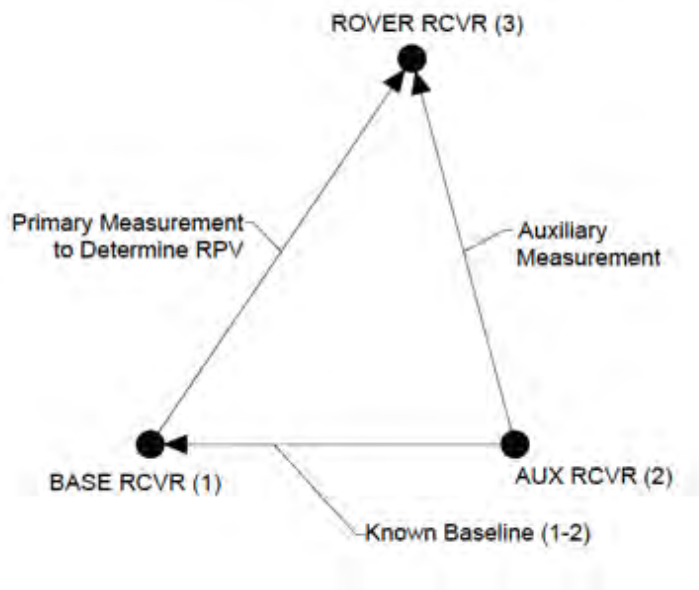

Figure 5.2: Vector representation of hardware configuration.

a, b, and r, representing the auxiliary, base, and rover receivers, respectively. The noise terms have been removed for brevity. The first step in the derivation is recognizing that the vector between the rover and the auxiliary receiver is the difference between the vectors between the rover and base, and the auxiliary and base shown in (5.1) and (5.5).

$$\Delta\rho^j_{r,a} = \Delta\rho^j_{r,b} - \Delta\rho^j_{a,b} \tag{5.1}$$

The actual single-difference measurement models between the rover and base is given in (5.4) and (5.8). This may be approximated with the single-difference measurements between the rover and auxiliary receivers with the addition of estimates of clock bias, relative integer ambiguities, and RPV between the auxiliary and base shown in (5.3) and (5.7).

$$\Delta\rho^j_{a,b} = \vec{a}_b\vec{r}_{a,b} + cb_{a,b} \tag{5.2}$$

$$\Delta\tilde{\rho}^j_{r,b} = \Delta\rho^j_{r,a} + \vec{a}_b\vec{r}_{a,b} + cb_{a,b} \approx \vec{a}_b\vec{r}_{r,b} + cb_{r,b} \tag{5.3}$$

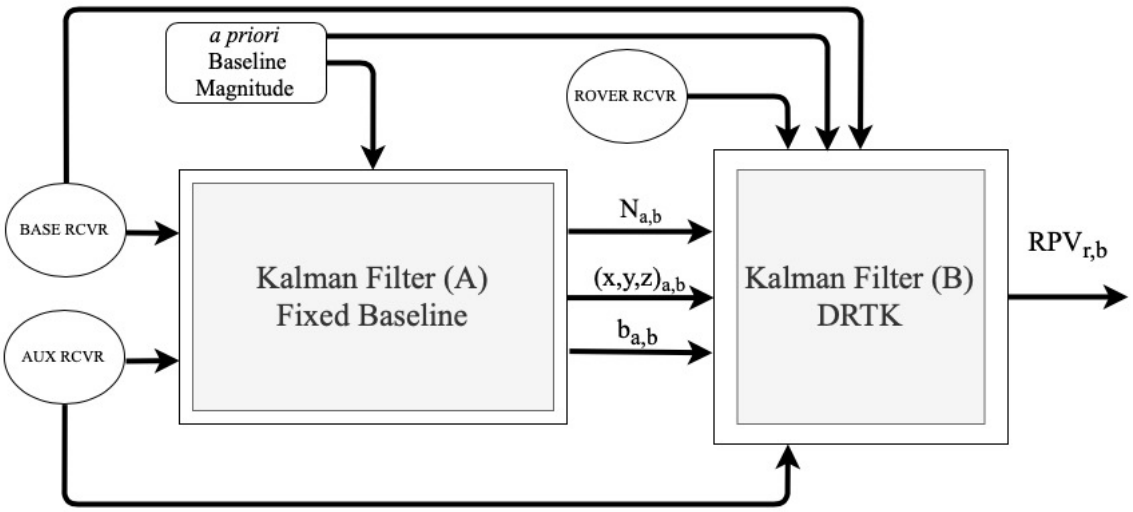

Figure 5.3: Description of cascaded Kalman filter architecture.

$$\Delta\rho^{j}_{r,b} = \vec{a}_b\vec{r}_{r,b} + cb_{r,b} \tag{5.4}$$

$$\Delta\phi^{j}_{r,b} = \Delta\phi^{j}_{r,b} - \Delta\phi^{j}_{a,b} \tag{5.5}$$

$$\Delta\phi^{j}_{a,b} = \vec{a}_b\vec{r}_{a,b} + \lambda N_{a,b} + cb_{a,b} \tag{5.6}$$

$$\Delta\tilde{\phi}^{j}_{r,b} = \Delta\phi^{j}_{r,a} + \vec{a}_b\vec{r}_{a,b} + \lambda N_{a,b} + cb_{a,b} + \epsilon^{j}_{r,b+a,b+r,a} \approx \vec{a}_b\vec{r}_{r,b} + \lambda N_{r,b} + cb_{r,b} \tag{5.7}$$

$$\Delta\phi^{j}_{r,b} = \vec{a}_b\vec{r}_{r,b} + \lambda N_{r,b} + cb_{r,b} \tag{5.8}$$

The measurement vector for the Kalman filter is given in (5.9). The tildes above ρ and ϕ represent derived measurements. The additional noise on the derived measurements must be accounted for in the $\mathbf{R}$ matrix of the Kalman filter given in (5.11), where $\sigma_{D\rho}$ represents the noise introduced by the error in estimation of the RPV and clock between the base and auxiliary receiver, and $\sigma_{D\phi}$ represents $\sigma_{D\rho}$ plus error in estimation of the float integer

ambiguities. $\sigma_{D\rho}$ and $\sigma_{D\phi}$ were determined empirically to be approximately 2 m with the dominant error sources being the error in estimation of $\lambda N_{r,b}$ and $cb_{r,b}$.

$$\mathbf{z} = \begin{bmatrix} \Delta\rho_{r,b}^{1\ldots m} \\ \Delta\tilde{\rho}_{r,b}^{1\ldots m} \\ \Delta\phi_{r,b}^{1\ldots m} \\ \Delta\tilde{\phi}_{r,b}^{1\ldots m} \end{bmatrix} \tag{5.9}$$

Including the additional measurements is done in the same procedure as given in Chapter 3. The $\mathbf{G}$ matrix is now $(4m \times 4)$ representing twice the pseudorange and twice the carrier phase measurements on the L1 frequency. The left nullspace of $\mathbf{G}$ is computed and augments the observation matrix $\mathbf{H}$ as shown in (5.10).

$$\mathbf{H} = \mathbf{L} \begin{bmatrix} 0_{2m\times m} & 0_{2m\times m} \\ \lambda_{L1} I_{m\times m} & 0_{m\times m} \\ 0_{m\times m} & \lambda_{L1} I_{m\times m} \end{bmatrix} \tag{5.10}$$

$$\mathbf{R} = \mathbf{L} \begin{bmatrix} \sigma_{r_{DLL}}^2 + \sigma_{b_{DLL}}^2 & 0 & 0 & 0 \\ 0 & \sigma_{r_{DLL}}^2 + \sigma_{a_{DLL}}^2 + \sigma_{D\rho}^2 & 0 & 0 \\ 0 & 0 & \sigma_{r_{PLL}}^2 + \sigma_{b_{PLL}}^2 & 0 \\ 0 & 0 & 0 & \sigma_{r_{PLL}}^2 + \sigma_{a_{PLL}}^2 + \sigma_{D\phi}^2 \end{bmatrix} \mathbf{L^T} \tag{5.11}$$

The system model remains the same as the conventional DRTK model given in Section 3.1.2.1.2. with the key difference in that the state covariance matrix, $\mathbf{P}$, is $(m \times m)$ because the only relative integer ambiguity states estimated are those between the rover and base on the L1 frequency. Initialization of the filter is performed with (3.20). The implementation steps are identical to the details in Section 3.1.2.2-3.1.2.4.

5.2 Experimentation and Results

Experimental data was collected at 1 Hz in the area shown in Figure 4.5. Three dual-frequency NovAtel receivers were used to collect data on the L1 frequency with NovAtel pinwheel antennas. The two vehicles used for data collection in a leader-follower configuration can be seen in Figure 5.4. The Infiniti G35 served as the leader vehicle, while the Lincoln Mkz served as the rover. The base and auxiliary receivers were located on the Lincoln Mkz. The rover receiver was located on the Infiniti G35. The gap distance between vehicles was never greater than 50 m. RTK corrections for truth comparison were provided by GrafNav. All algorithms were implemented in MATLAB.

Figure 5.4: Lincoln Mkz and Infiniti G35 in the leader-follower configuration used for data collection.

5.2.1 LAMBDA and TTFF

The results of the experiment showed that the derived measurements benefited estimation of the integer ambiguities. A summary of the LAMBDA ratio passing rates is given in Table 5.1. The LAMBDA ratio threshold used was 3. These statistics were generated the same way as in Chapter 4 by initializing the filter at 100 different epochs within the experimental data. FAD+DRTK with L1 approached the performance of DRTK with (L1-L2) by fixing within three epochs (see Table 4.3). DRTK with L1 fixed within six epochs. Table 5.2 shows improvement in the initial estimate determined by the value of the LAMBDA ratio with FAD+DRTK; however, neither FAD+DRTK or DRTK matched the performance of DRTK with (L1-L2) (see Table 4.4).

Table 5.1: Statistics on LAMBDA Ratio Passing Rate with L1

Method	**% Pass on 1^{st} Epoch**	**% Pass on 2^{nd} Epoch**	**% Pass on 3^{rd} Epoch**
DRTK	2	61	77
FAD+DRTK	35	86	100

Table 5.2: Statistics on LAMBDA Ratio Results with L1

Method	**Median λ_R on 1^{st} Epoch**	**Max λ_R on 1^{st} Epoch**	**Min λ_R on 1^{st} Epoch**
DRTK	1.93	3.16	1.00
FAD+DRTK	2.59	5.02	1.22

5.2.2 Accuracy of the Derived Measurements

The accuracy of the derived single-difference pseudorange and carrier-phase measurements were compared against the actual single-difference pseudorange and carrier-phase measurements. Figures 5.5 and 5.6 show that the derived measurements track the actual measurements, but not as closely as measurements on the L2 frequency. This can be attributed to the error in estimation of $\lambda N_{r,b}$ and $cb_{r,b}$ used to derive the additional measurements. Additionally, it is important to recognize that measurements made on the L2

frequency are higher in quality than those on the L1 frequency. The L2 frequency is higher than the L1 frequency (see Table 2.1); therefore, L2 is altered less by atmospheric effects. Therefore, five L1 and five derived L1 measurements is not equivalent to five L1 and five L2 measurements.

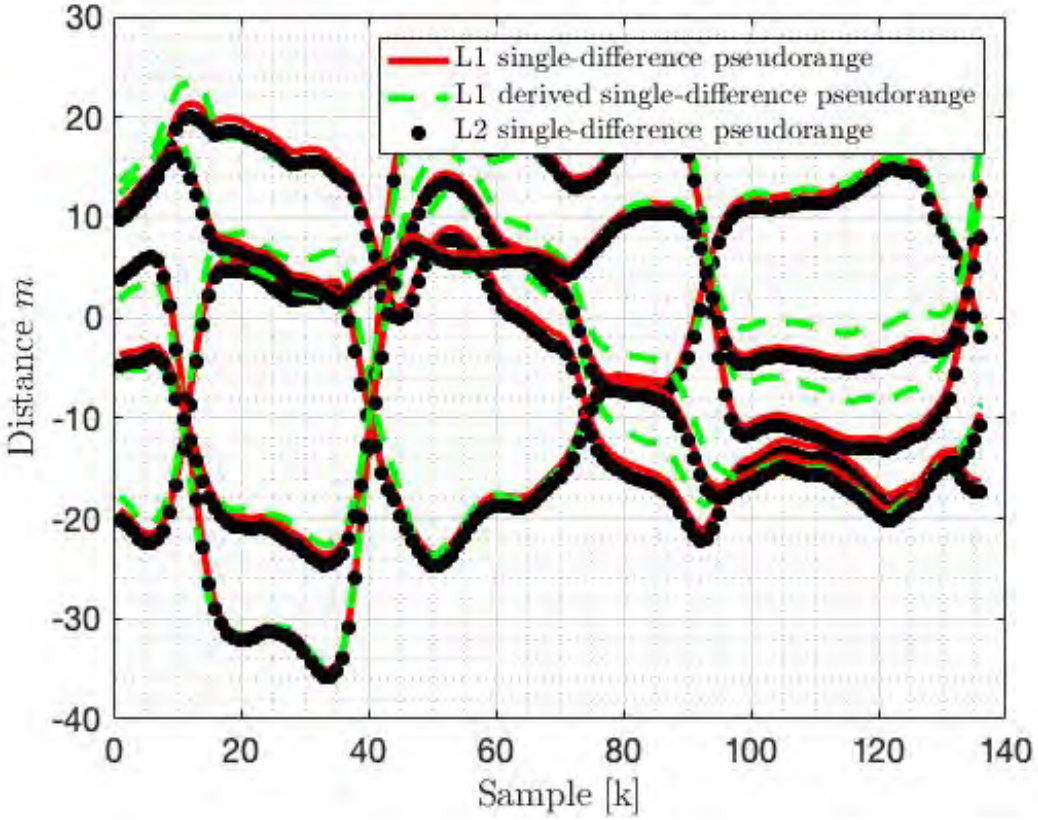

Figure 5.5: Comparison of the L1, L2, and derived L1 single-difference pseudorange measurements between the rover and base antenna.

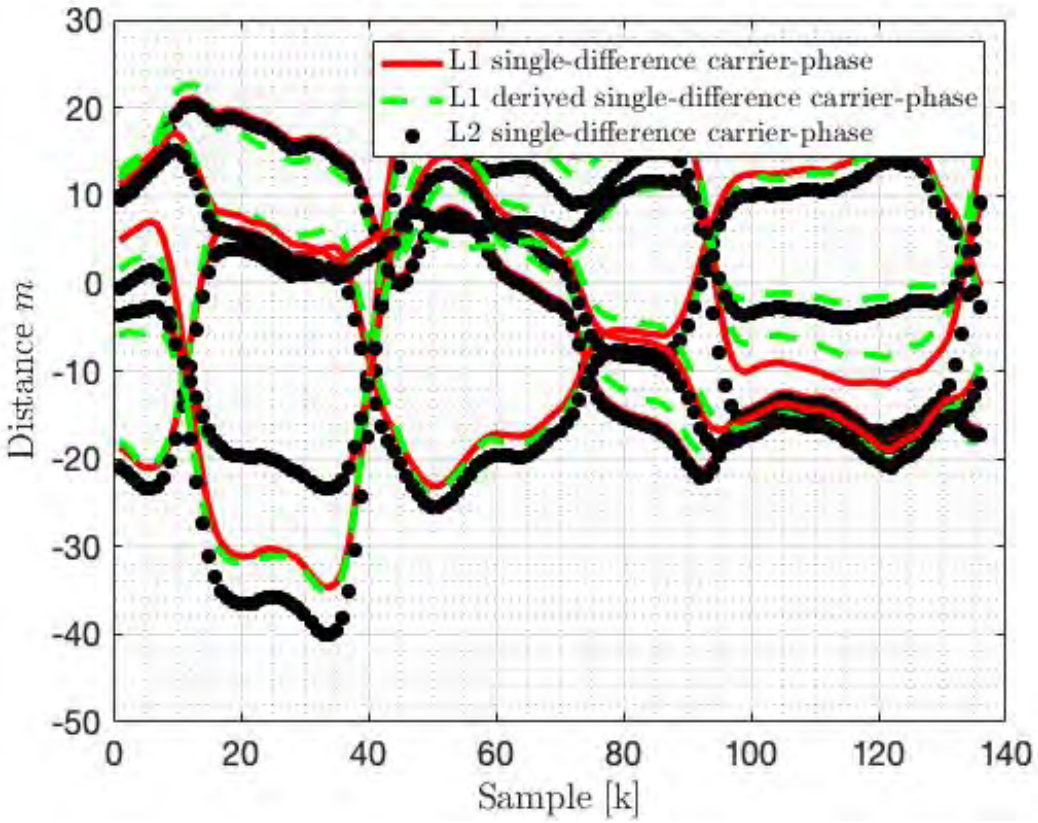

Figure 5.6: Comparison of the L1, L2, and derived L1 single-difference carrier-phase measurements between the rover and base antenna.

A summary of error statistics on the derived L1 measurements and actual L1 measurements compared against L2 measurements are tabulated in Tables 5.3 and 5.4. These statistics were generated by taking the difference in derived L1 measurements and the L2 measurements, and the difference in the actual L1 measurements and the L2 measurements on each respective receiver channel (i.e. SV PRN). The rms error of the derived L1 and actual L1 measurements are similar for both pseudorange and carrier-phase; however, they differ in variance, which is accounted for in (5.11).

Table 5.3: Error Statistics of the difference in Actual and Derived L1 single-difference pseudorange measurements compared against L2 single-difference pseudorange measurements.

SV PRN	**L1 C/A RMSE** (m)	**L1 C/A** $\sigma(m)$	**Derived L1 C/A RMSE** (m)	**Derived L1 C/A** $\sigma(m)$
3	1.17	0.07	2.44	2.36
14	1.03	0.07	1.51	1.41
16	0.82	0.22	2.51	2.43
22	1.00	0.01	1.76	1.64
26	0.95	0.06	1.74	1.67

Table 5.4: Error Statistics of the difference in Actual and Derived L1 single-difference carrier-phase measurements compared against L2 single-difference carrier-phase measurements.

SV PRN	**L1 RMSE** (m)	**L1** $\sigma(m)$	**Derived L1 RMSE** (m)	**Derived L1** $\sigma(m)$
3	0.79	0.007	2.34	2.35
14	2.34	0.007	1.39	1.38
16	5.45	0.010	2.45	2.46
22	1.96	0.006	1.63	1.64
26	0.19	0.007	1.62	1.61

5.2.3 Error Analysis

Both DRTK and FAD+DRTK provided the same rms error values once fixed, since both techniques use the true carrier phase measurement between the rover and base. A summary of error statistics is given in Table 5.5. Error plots are provided in Figure 5.8 and Figure 5.10. Note the error plots include the initial float solution before fixing. Finally, Figure 5.7 and Figure 5.9 show that the FAD+DRTK solution tracks the RTK solution, as expected.

Table 5.5: Error Statistics on DRTK and FAD+DRTK

Method	RMSE (cm)	Var (cm^2)
DRTK	0.40	0.11
FAD+DRTK	0.40	0.11

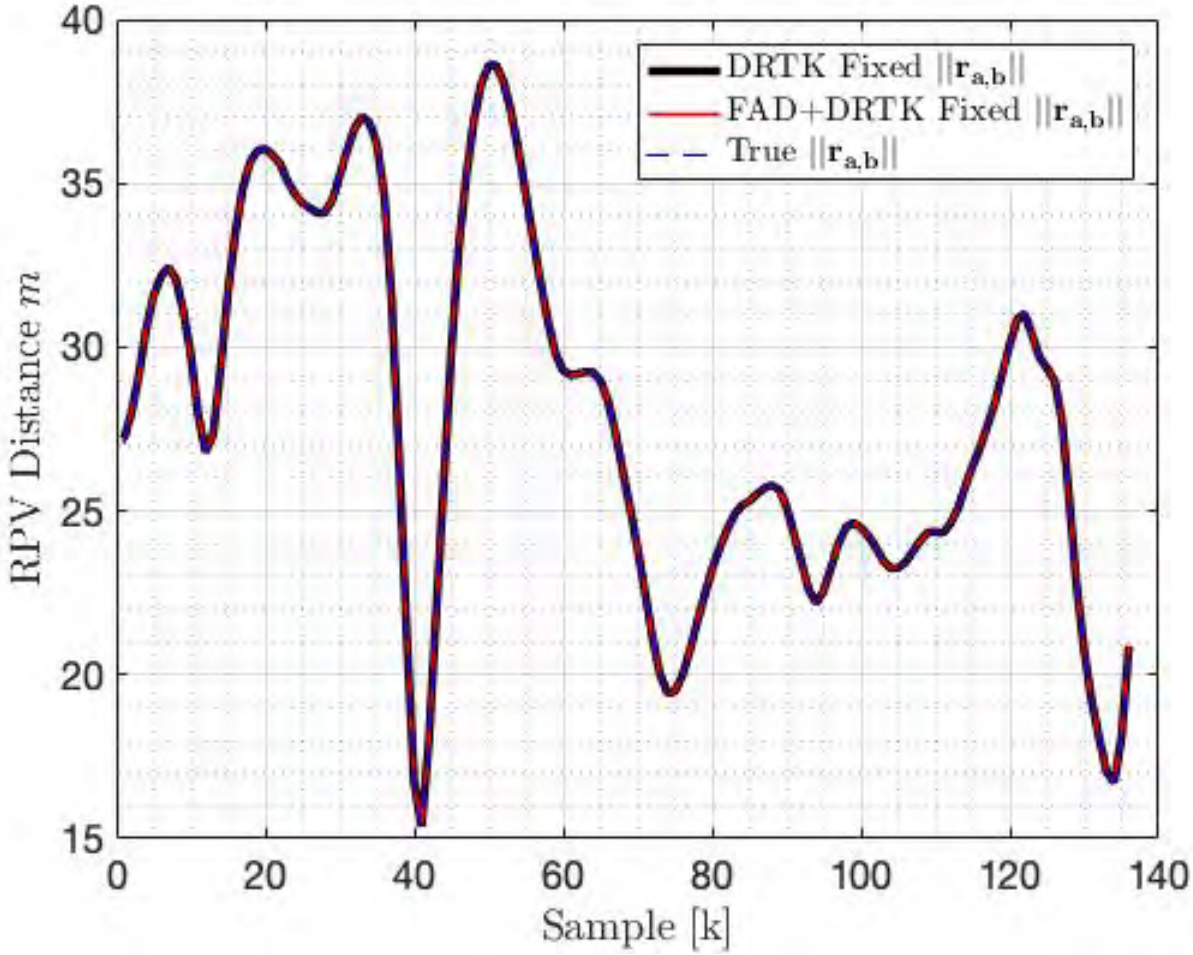

Figure 5.7: HPRPV magnitude estimate compared with RTK.

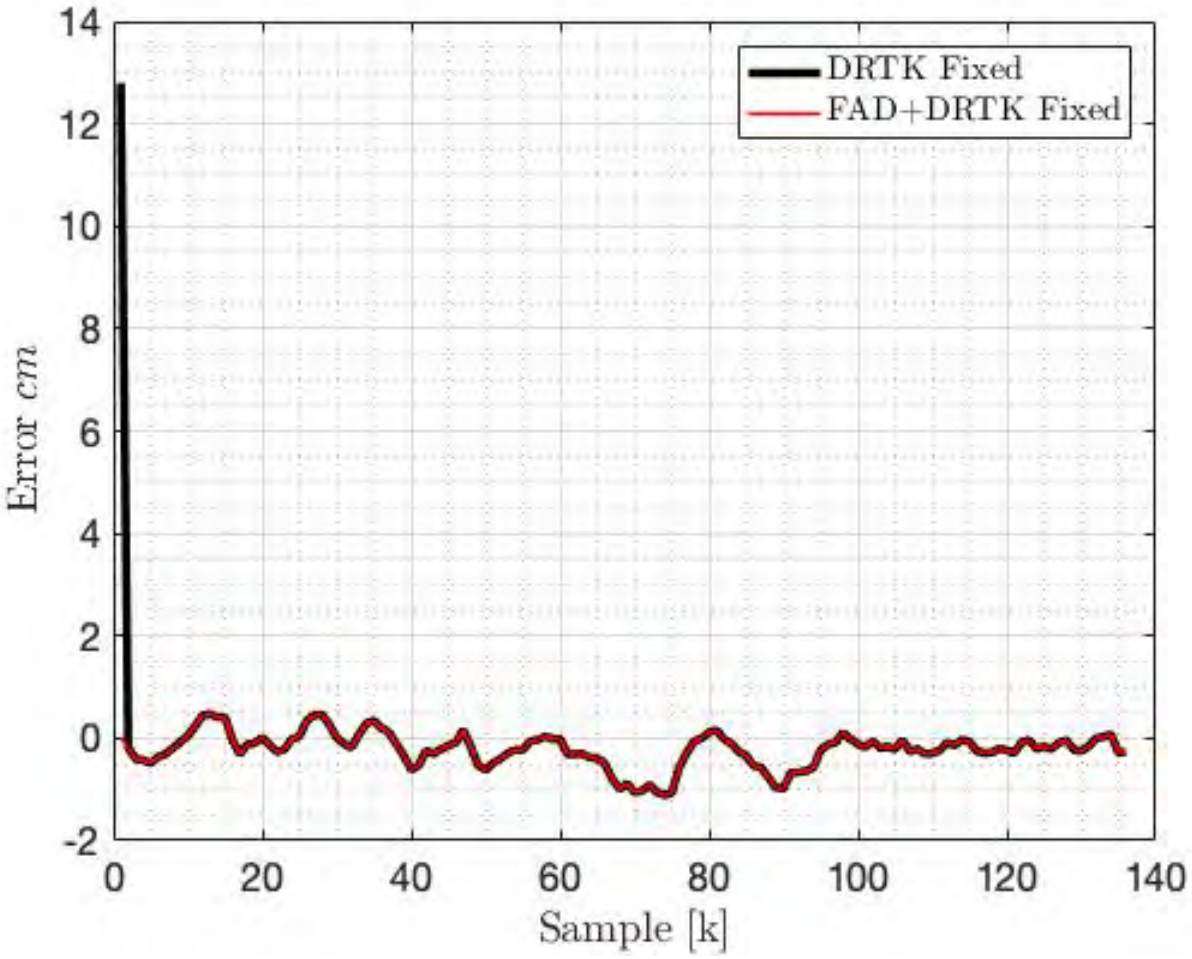

Figure 5.8: Error in HPRPV magnitude estimate.

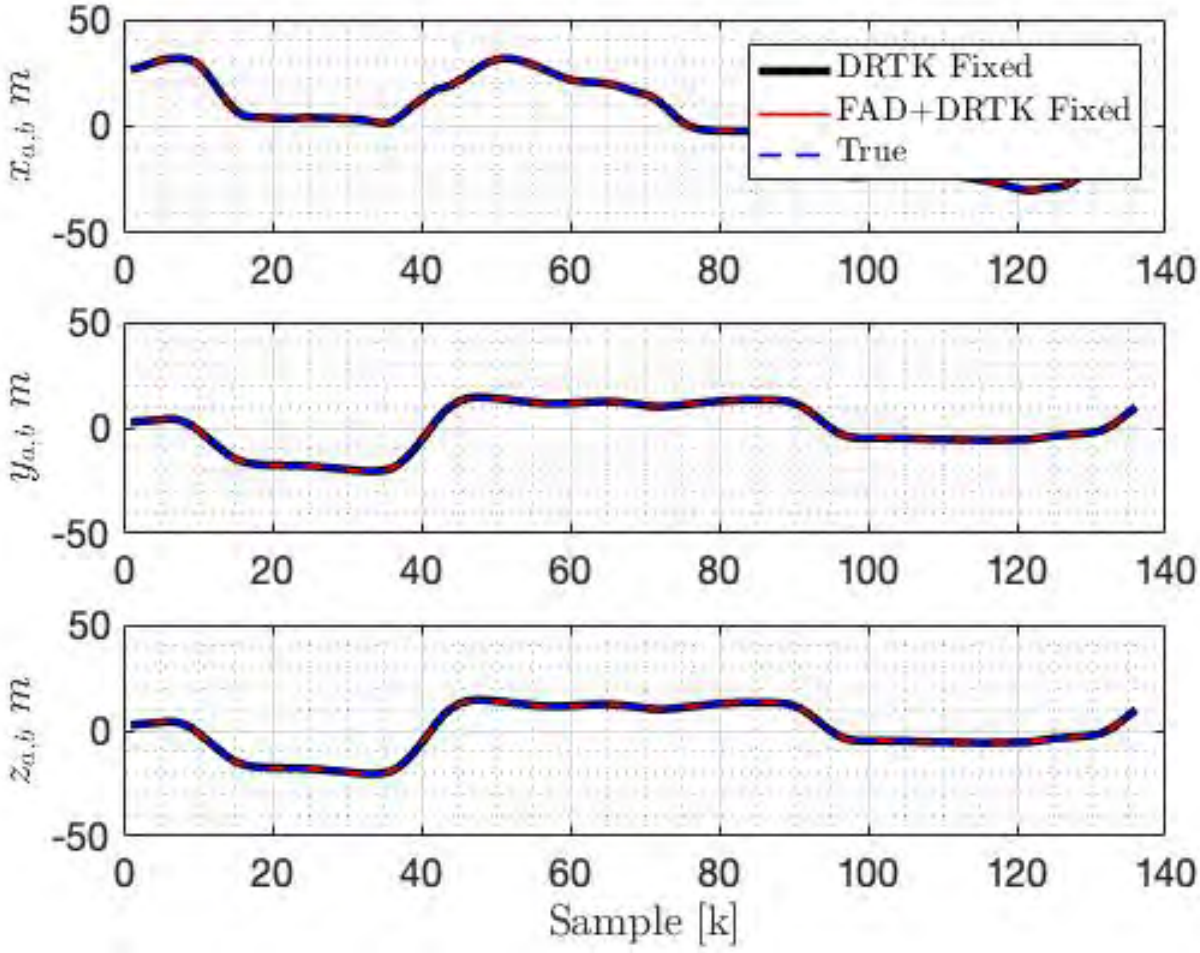

Figure 5.9: HPRPV estimates compared with RTK.

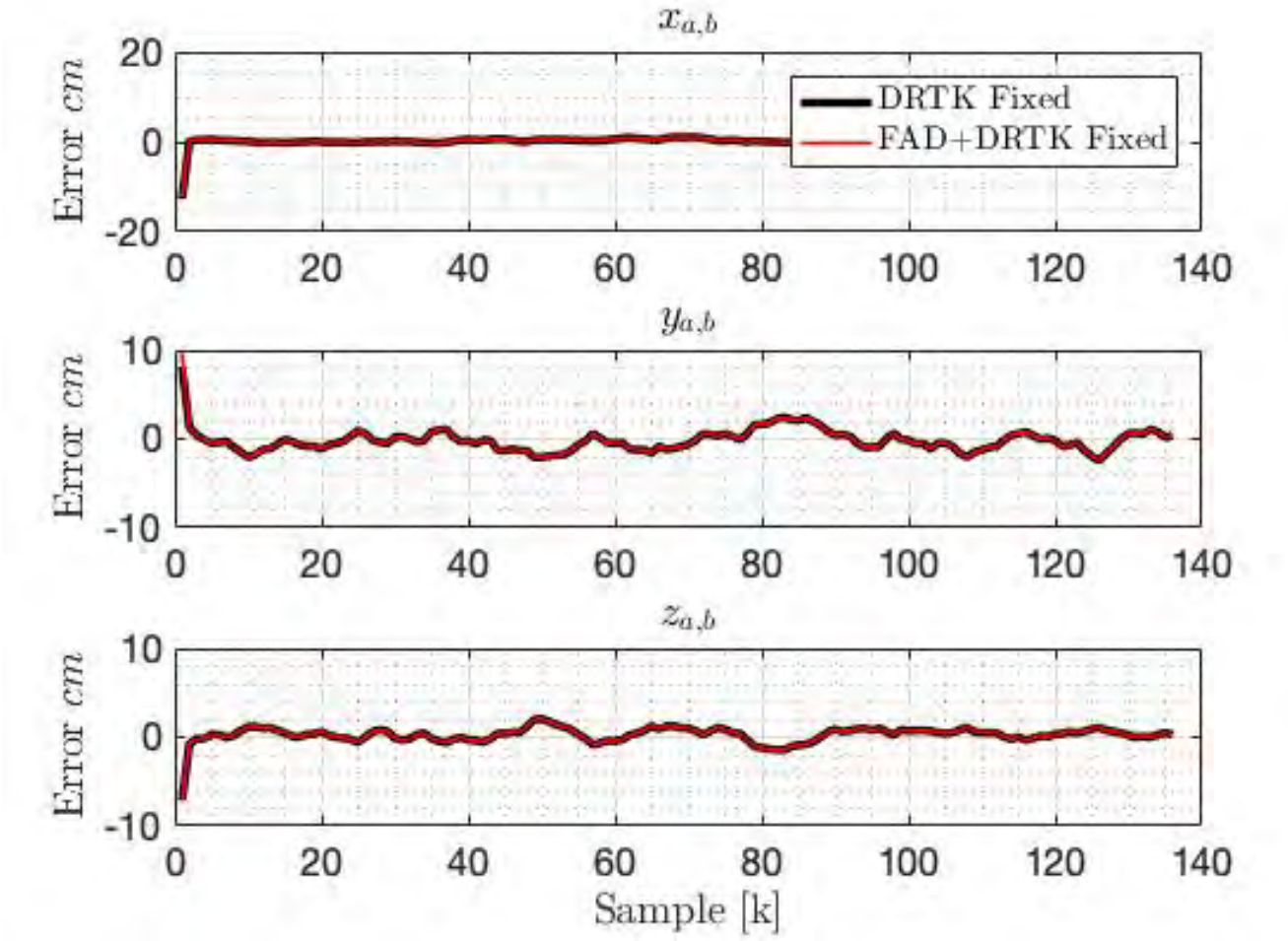

Figure 5.10: Error in HPRPV estimates.

5.3 Conclusions

Combining measurements between three receivers in the described FAD+DRTK cascaded Kalman filter with L1 framework provided a faster TTFF and higher LAMBDA ratios on average than DRTK with L1. Both techniques, once fixed, provide centimeter level relative positioning solutions. The FAD+DRTK technique gives an option for users to employ low-cost single-frequency receivers to approach dual-frequency receiver performance in applications where low-cost sensing for relative positioning is desired. The hardware cost of

three single-frequency receivers will be thousands of dollars less than two high quality dual-frequency receivers, with the added benefit of the ability to determine vehicle attitude. This approach ultimately offers relative positioning and attitude determination for collaborative navigation at a low-cost for the cost sensitive automotive industry.

Chapter 6

Conclusions and Future Work

6.1 Summary

Chapter 1 motivated the need for GPS based positioning in autonomous convoying applications by describing the strengths and weaknesses of common sensors employed in autonomy. GPS was shown to serve as a correction for relative sensors and provides an independent measurement of velocity and odometry with high-accuracy. Additionally, the ability of accurate GPS based relative positioning was presented. A brief survey of absolute and relative sensors was presented to depict the current state of the art. This led to a more detailed description of GPS. Next, prior work in the field of carrier based GPS relative positioning was presented along with the contributions of this thesis.

Chapter 2 presented a brief history of GPS and its described purpose by the DoD. The three segments of GPS, Space, Control, and User, were discussed to convey the multifaceted collaboration required for operation and the unique error sources contributed by each segment. Within the User segment section, the GPS measurement models of pseudorange and carrier phase were presented with their expected accuracy and individual components. The method of measurement generation by the GPS receiver was briefly discussed. Finally, a 50 *min* experiment was conducted to validate the accuracy of standalone positioning with the SPS of GPS.

Chapter 3 introduced the DRTK (L1-L2) algorithm. The DRTK technique was shown to provide RTK quality relative positioning solutions. The LAMBDA method was presented to describe the method used to fix double-difference carrier phase floating point ambiguities to integers, and to discuss the LAMBDA ratio's use for validation of solutions. The least squares estimation technique was shown to be used to determine the RPV once integer

ambiguities were fixed. An experiment was then conducted to validate the expected accuracy of DRTK and the resulting LAMBDA ratio results. Lastly, the limitation of DRTK to provide solutions only when both receivers have common satellites in view was discussed to compare availability of solutions to RTK.

Chapter 4 introduced the fixed attitude-baseline DRTK (FAD) technique used to fix integer ambiguities between antennas in a fixed attitude baseline configuration on a moving platform. The inclusion of an *a priori* baseline magnitude for constrained Kalman filtering was then presented. The FAD technique was shown to outperform DRTK with regards to TTFF and LAMBDA ratio results. Both FAD and DRTK were shown to provide the same HPRPV solution once integers were fixed.

Chapter 5 described the inclusion of relative integer ambiguity estimates, relative clock bias, and RPV states estimated by FAD to derive additional measurements to aid DRTK relative positioning with single-frequency receivers. The cascaded Kalman filter with FAD and DRTK was presented along with a derivation of the additional measurements derived from three independent GPS receivers. The FAD+DRTK technique was shown to provide a faster TTFF and higher LAMBDA ratios on average than DRTK. Both FAD+DRTK and DRTK were shown to provide the same RPV solution once integers were fixed correctly. FAD+DRTK was recommended as an option to the cost sensitive automotive industry to provide a lower cost hardware implementation for relative positioning in collaborative navigation applications like autonomous convoying.

6.2 Conclusions

In conclusion, carrier based GPS relative positioning techniques for autonomous convoying were covered. Three estimation schemes were presented with a focus on TTFF and confidence in solution gauged by the LAMBDA ratio result. DRTK, FAD, and DRTK+FAD were all shown to provide relative positioning with accuracy of approximately 2 cm. DRTK is

the best relative positioning option for applications where dual-frequency receivers are available, a base station is unavailable, and platform attitude isn't a concern. FAD is an option for applications where dual or single-frequency receivers are available and the user requires GPS aided attitude estimation. When using single-frequency receivers, FAD+DRTK provided a fixed integer solution within three epochs for every initialization, while DRTK provided a fixed integer solution within six epochs for every initialization. The FAD+DRTK TTFF was similar to dual-frequency DRTK in that fixed integer solutions were available within three epochs but differed in the percentage of fixed integer solutions available within the first and second epochs. Finally, DRTK+FAD is shown to be a good option for users sensitive to hardware cost that desire attitude estimation and relative positioning between vehicles. All carrier based GPS estimation schemes presented provide *cm* level relative positioning.

6.3 Future Work

6.3.1 FAD for Towed Implement Control

Agricultural implement control requires knowledge of the position of the towed implement. This can be achieved with a receiver fixed to the implement receiving RTK correction or hitch angle measurements made by an optical encoder. Previous work using the DRTK algorithm was presented in [46]. The FAD technique can aid this estimation by applying an *a priori* baseline magnitude constraint when the velocity vector of the implement and the tractor are aligned determined by GPS 3D velocity measurements. Additionally, in a tractor trailer convoy, trailer position knowledge is useful for control. The same technique may also be applied for this application.

6.3.2 Orientation and Distance Between Antennas

A comprehensive comparison of the effect of baseline attitude configurations of different distances and orientations should be performed. A shorter baseline should result in better

performance because correlation of errors increases with decreasing distance between antennas. However, decreasing the distance between the fixed attitude-baseline affects geometric diversity of measurements, which may harm integer ambiguity resolution between convoying vehicles. Additionally, orientation of the baseline attitude on the platform affects the observability of the attitude states when only two antennas are used.

6.3.3 Validation with Low-Cost Receivers and Antennas

All work presented in this thesis used measurements from NovAtel pinwheel antennas that perform similarly to choke ring antennas and high-quality GPS receivers. The work in this thesis should be validated using low-cost patch antennas and single-frequency receivers.

6.3.4 The Use of an *a priori* Baseline Magnitude on Each Convoying Vehicle

The FAD technique described in Chapter 4 could be implemented on each convoying vehicle, given that each vehicle is configured with a fixed attitude-baseline of antennas. The low-cost of single-frequency receivers would justify this choice, because four single-frequency receivers would still be less expensive than two dual-frequency antennas by thousands of dollars. The FAD+DRTK technique described in Chapter 5 could then be used to derive more additional measurements to effectively triple the number of available measurements. A study should be conducted to determine if integer ambiguity resolution performance is improved with this approach.

6.3.5 Cascaded vs. Centralized Approach

The work presented in Chapter 5 used a centralized approach to derive additional measurements. A study should be performed to see if a centralized Kalman filter approach offers any benefit.

Bibliography

[1] Wsx2. [Online]. Available: https://commons.wikimedia.org/w/index.php?curid=2356776

[2] "Control segment." [Online]. Available: https://www.gps.gov/systems/gps/control/

[3] N. Dilmen. [Online]. Available: https://commons.wikimedia.org/w/index.php?curid=33689487

[4] P. Groves, *Principles of GNSS, Interial, and Multisensor Integrated Navigation Systems*, 1st ed. Boston, MA: Artech House, 2008.

[5] E. Kaplan and C. Hegarty, *Understanding GPS: principles and applications*. Artech house, 2005.

[6] [Online]. Available: https://www.navcen.uscg.gov/?Do=constellationstatus

[7] D. Barrie, *Supernavigators: Exploring the Wonders of how Animals Find Their Way*. The Experiment, 2019.

[8] N. Kehtarnavaz, N. Griswold, and J. Lee, "Visual control of an autonomous vehicle (bart)-the vehicle-following problem," *IEEE Transactions on Vehicular Technology*, vol. 40, no. 3, p. 654–662, 1991.

[9] J. Davis, A. Animashaun, E. Schoenherr, and K. Mcdowell, "Evaluation of semi-autonomous convoy driving," *Journal of Field Robotics*, vol. 25, no. 11-12, p. 880–897, 2008.

[10] D. T. Anderson, J. Lee and R. B. Schoenberger, "Using real-time vision to control a convoy of semi-autonomous unmanned vehicles," in *AUVSI Unmanned Systems North America Conference 2006*, 2006.

[11] H. Humphreys and D. Bevly, "Computational fluid dynamic analysis of a generic 2 truck platoon," SAE Technical Paper, Tech. Rep., 2016.

[12] J. I. Bowditch, *American practical navigator*. US Government Printing Office, 1880, no. 9.

[13] S. Huang and G. Dissanayake, "Robot localization: An introduction," *Wiley Encyclopedia of Electrical and Electronics Engineering*, pp. 1–10, 1999.

[14] J. Borenstein, H. Everett, L. Feng, and D. Wehe, "Mobile robot positioning - sensors and techniques," *Journal of Robotic Systems*, vol. 14, no. 4, pp. 231–249, 1995.

[15] Y. Zhao, *Vehicle location and navigation systems*, 1997.

[16] W. Lowrie, *Fundamentals of geophysics*. Cambridge university press, 2007.

[17] B. W. Parkinson and J. Spilker, *Global positioning system: theory and applications*. American Institute of aeronautics and astronautics, 1996.

[18] U. DoD, "Global positioning system standard positioning service performance standard," *Assistant secretary of defense for command, control, communications, and intelligence*, 2008.

[19] Y. Feng and J. Wang, "Gps rtk performance characteristics and analysis," *Journal of Global Positioning Systems*, vol. 7, no. 1, pp. 1–8, 2008.

[20] J. C. Tuthill and E. Azim, "Proprioception," *Current Biology*, vol. 28, no. 5, pp. R194–R203, 2018.

[21] P. Misra and P. Enge, "Global positioning system: signals, measurements and performance second edition," *Massachusetts: Ganga-Jamuna Press*, 2006.

[22] T. D. Gillespie, "Fundamentals of vehicle dynamics," SAE Technical Paper, Tech. Rep., 1992.

[23] J. Borenstein and L. Feng, "Measurement and correction of systematic odometry errors in mobile robots," *IEEE Transactions on robotics and automation*, vol. 12, no. 6, pp. 869–880, 1996.

[24] ——, "Umbmark: A method for measuring, comparing, and correcting dead-reckoning errors in mobile robots," University of Michigan, Tech. Rep., 1994.

[25] S. Martin, "Closely coupled gps/ins relative positioning for automated vehicle convoys," Master's thesis, Auburn University, 2011.

[26] J. Wagner, "From bohnenberger's machine to integrated navigation systems, 200 years of inertial navigation," *Photogrammetric Week, Wichmann Verlag, Heidelberg*, 2005.

[27] B. Powell, "On the theory of m. foucault's gyroscope experiments," *Monthly Notices of the Royal Astronomical Society*, vol. 15, p. 182, 1855.

[28] W. Rindler, *Essential relativity: special, general, and cosmological*. Springer Science & Business Media, 2012.

[29] E. F. Taylor and J. A. Wheeler, *Spacetime physics*. Macmillan, 1992.

[30] D. Pierce, "Incorporation of a foot-mounted imu for multi-sensor pedestrian navigation," Master's thesis, Auburn University, 2016.

[31] T. N. Ray, "Pedestrian navigation using particle filtering and a priori building maps," Master's thesis, Auburn University, 2019.

[32] C. Fries, P. Burger, J. Kallwies, B. Naujoks, T. Luettel, and H.-J. Wuensche, "How mucar won the convoy scenario at elrob 2016," in *2017 IEEE 20th International Conference on Intelligent Transportation Systems (ITSC)*. IEEE, 2017, pp. 1–7.

[33] T. Féraud, P. Checchin, R. Aufrère, and R. Chapuis, "Communicating vehicles in convoy and monocular vision-based localization," *IFAC Proceedings Volumes*, vol. 43, no. 16, pp. 73–78, 2010.

[34] R. Chatila and J.-P. Laumond, "Position referencing and consistent world modeling for mobile robots," in *Proceedings. 1985 IEEE International Conference on Robotics and Automation*, vol. 2. IEEE, 1985, pp. 138–145.

[35] P. Fritsche, S. Kueppers, G. Briese, and B. Wagner, "Radar and lidar sensorfusion in low visibility environments." in *ICINCO (2)*, 2016, pp. 30–36.

[36] L. Mullen and V. Contarino, "Hybrid lidar-radar: Seeing through the scatter," *IEEE Microwave Magazine*, vol. 1, no. 3, p. 42–48, 2000.

[37] M. Himmelsbach, A. Mueller, T. Lüttel, and H.-J. Wünsche, "Lidar-based 3d object perception," in *Proceedings of 1st international workshop on cognition for technical systems*, vol. 1, 2008.

[38] C. Fries and H.-J. Wuensche, "Autonomous convoy driving by night: The vehicle tracking system," in *2015 IEEE International Conference on Technologies for Practical Robot Applications (TePRA)*. IEEE, 2015, pp. 1–6.

[39] A. Schneider, Z. L. Celle, A. Lacaze, K.Murphy, M. D. Giorno, and R. Close, "Sensor study for high speed autonomous operations," in *Next-Generation Robotics II; and Machine Intelligence and Bio-inspired Computation: Theory and Applications IX*, vol. 9494. International Society for Optics and Photonics, 2015, p. 949408.

[40] B. W. Remondi, "Performing centimeter-level surveys in seconds with gps carrier phase: initial results," *Navigation*, vol. 32, no. 4, pp. 386–400, 1985.

[41] W. Falkenberg, T. Ford, J. Neumann, P. Fenton, M. E. Cannon, and G. Lachapelle, "Precise real-time kinematic differential gps using a cellular radio modem," *Proceedings of PLANS '92, The Institute of Electrical and Electronics Engineers, New York*, p. 391, 1992.

[42] S. J. Comstock, "Development of a low-latency, high data rate, differential gps relative positioning system for uav formation flight control," AIR FORCE INST OF TECHNOLOGY WRIGHT-PATTERSON AFB OH GRADUATE SCHOOL OF ENGINEERING AND MANAGEMENT, Tech. Rep., 2006.

[43] S. C. Felter and N. E. Wu, "A relative navigation system for formation flight," *IEEE Transactions on Aerospace and Electronic Systems*, vol. 33, no. 3, pp. 958–967, 1997.

[44] S. Khanafseh, B. Kempny, and B. Pervan, "New applications of measurement redundancy in high performance relative navigation systems for aviation," in *Proceedings of the 19th International Technical Meeting of the Satellite Division of the Institute of Navigation (ION GNSS 2006)*, 2006, pp. 3024–3034.

[45] S. Dogra, J. Wright, and J. Hansen, "Sea-based jpals relative navigation algorithm development," in *Proceedings of the 18th International Technical Meeting of the Satellite Division of the Institute of Navigation ION GNSS*, 2005, p. 2871.

[46] W. Travis, D. Hodo, D. Bevly, and J. Hung, "Ugv trailer position estimation using a dynamic base rtk system," in *AIAA Guidance, Navigation and Control Conference and Exhibit*, 2008, p. 7442.

[47] W. Travis and D. M. Bevly, "Trajectory duplication using relative position information for automated ground vehicle convoys," in *2008 IEEE/ION Position, Location and Navigation Symposium*. IEEE, 2008, pp. 1022–1032.

[48] A. Sperl, "Joint RTK and Attitude Determination," Master's thesis, Technische Universität München, 2015.

[49] *NovAtel OEM4 Volume 1 Installation and Operation*, NovAtel, Hexagon Calgary Campus, 10921 14th Street NE, Calgary, Alberta, Canada, dec 2005.

[50] J. A. Gubner, *Probability and random processes for electrical and computer engineers*. Cambridge University Press, 2006.

[51] R. G. Brown, P. Y. Hwang *et al.*, *Introduction to random signals and applied Kalman filtering*. Wiley New York, 1992, vol. 3.

[52] J. J. Tuma, *Engineering mathematics handbook*. McGraw-Hill, 1970.

[53] G. Strang, G. Strang, G. Strang, and G. Strang, *Introduction to linear algebra*. Wellesley-Cambridge Press Wellesley, MA, 1993, vol. 3.

[54] P. J. Teunissen, P. De Jonge, and C. Tiberius, "Performance of the lambda method for fast gps ambiguity resolution," *Navigation*, vol. 44, no. 3, pp. 373–383, 1997.

[55] P. J. Teunissen and S. Verhagen, "The gnss ambiguity ratio-test revisited: a better way of using it," *Survey Review*, vol. 41, no. 312, pp. 138–151, 2009.

[56] S. Verhagen and P. Teunissen, "On the foundation of the popular ratio test for gnss ambiguity resolution," in *Proceedings of the 17th International Technical Meeting of the Satellite Division of The Institute of Navigation (ION GNSS 2004)*. ION, 2004, pp. 2529–2540.

[57] K. Borre and G. Strang, *Algorithms for global positioning*. Wellesley-Cambridge Press Cambridge, 2012.

[58] W. Travis, S. M. Martin, D. W. Hodo, and D. M. Bevly, "Non-line-of-sight automated vehicle following using a dynamic base rtk system," *Navigation*, vol. 58, no. 3, pp. 241–255, 2011.

[59] S. Martin and D. M. Bevly, "Comparison of gps-based autonomous vehicle following using global and relative positioning," *International Journal of Vehicle Autonomous Systems*, vol. 10, no. 3, pp. 229–255, 2012.

[60] S. M. Martin, "Gps carrier phase tracking in difficult environments using vector tracking for precise positioning and vehicle attitude estimation," Ph.D. dissertation, Auburn University, 2017.

[61] C. E. Cohen, "Attitude determination using gps," *Stanford University, Ph. D. Dissertation, Department of Aeronautics and Astronautics*, 1992.

[62] D. Simon, *Optimal state estimation: Kalman, H infinity, and nonlinear approaches*. John Wiley & Sons, 2006.

[63] A. Gelb, *Applied optimal estimation*. MIT press, 1974.

[64] J. Kim, R. R. Rajkumar, and M. Jochim, "Towards dependable autonomous driving vehicles: a system-level approach," *ACM SIGBED Review*, vol. 10, no. 1, pp. 29–32, 2013.

[65] T. Takasu and A. Yasuda, "Evaluation of rtk-gps performance with low-cost single-frequency gps receivers," in *Proceedings of international symposium on GPS/GNSS*, 2008, pp. 852–861.

[66] T. T. Tabb, S. M. Martin, and D. Bevly, "Improved relative positioning for path following in autonomous convoys," in *NDIA Ground Vehicle Systems Engineering and Technology Symposium*.

[67] A. Bryson and D. Johansen, "Linear filtering for time-varying systems using measurements containing colored noise," *IEEE Transactions on Automatic Control*, vol. 10, no. 1, pp. 4–10, 1965.

Appendices

Appendix A

Current Active Satellites

The United States Department of Defense aims to guarantee a minimum of twenty-four active satellites within the Global Position System constellation. As of this writing, there are thirty-one active satellites, which can be found in Table A.1.

Table A.1: The current active satellites in the GPS constellation with outage date information as of June 7, 2019. (From: [6])

Plane	**PRN**	**Outage Date**
A	24	
A	31	
A	30	06 JUN 2019
A	7	
B	16	
B	25	
B	28	
B	12	
B	26	
C	29	
C	27	
C	8	
C	17	
C	19	
D	2	
D	1	
D	21	
D	6	
D	11	
D	18	02 JUN 2019
E	3	
E	10	
E	5	
E	20	
E	22	
F	32	
F	15	
F	9	
F	23	
F	14	
F	13	

Appendix B

Earth-Centered, Earth-Fixed Cartesian Coordinate System

The Earth-Centered, Earth-Fixed (ECEF) Cartesian coordinate system is widely used in navigation. As the name implies, the coordinate system rotates with the Earth. The origin is at the center of mass of the Earth. Simply described, The Z-axis coincides with the axis of rotation, and the X-axis coincides with the intersection of the *Mean Greenwich meridian* with the equatorial plane. However, the Earth's rotation axis is not fixed in relation to the Earth. The pole of rotation actually meanders in a roughly circular path several meters per year around the surface of the Earth. This phenomenon is known as *polar motion*. This polar motion alters the definition of the equatorial plane, therefore the entire coordinate system would be dynamic if this wasn't addressed. To resolve this polar motion issue, geodesists between the years of 1900 and 1905 defined an average position of the pole of rotation. This point, fixed to the Earth's crust, is known as the *Conventional Terrestrial Pole* (CTP). Figure B.1 offers a depiction of the ECEF coordinate frame.

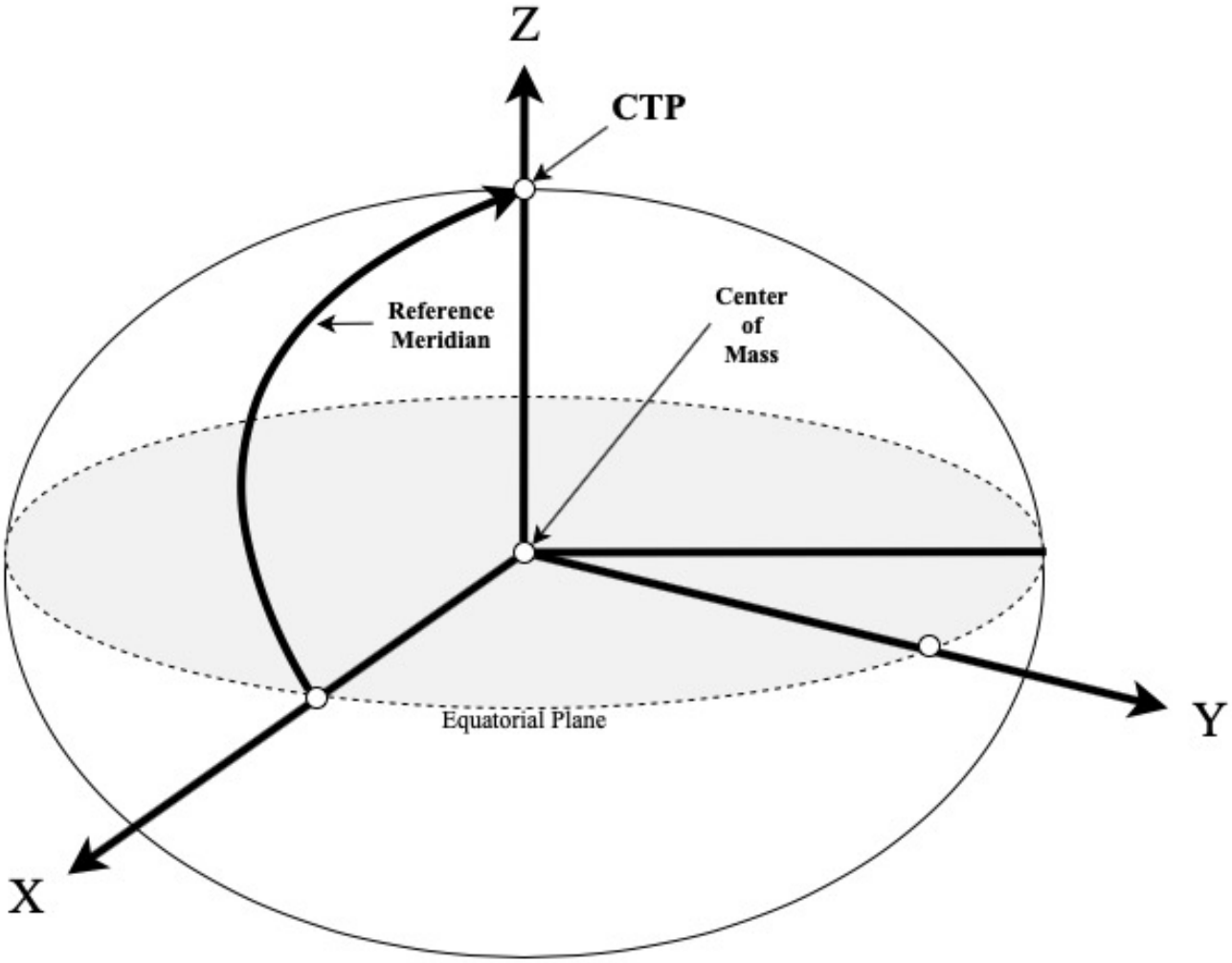

Figure B.1: Description of the earth-centered earth-fixed Cartesian coordinate system.